iScience

CellPress
OPEN ACCESS

Article

Au@Pt Nanotubes within CoZn-Based Metal-Organic Framework for Highly Efficient Semi-hydrogenation of Acetylene

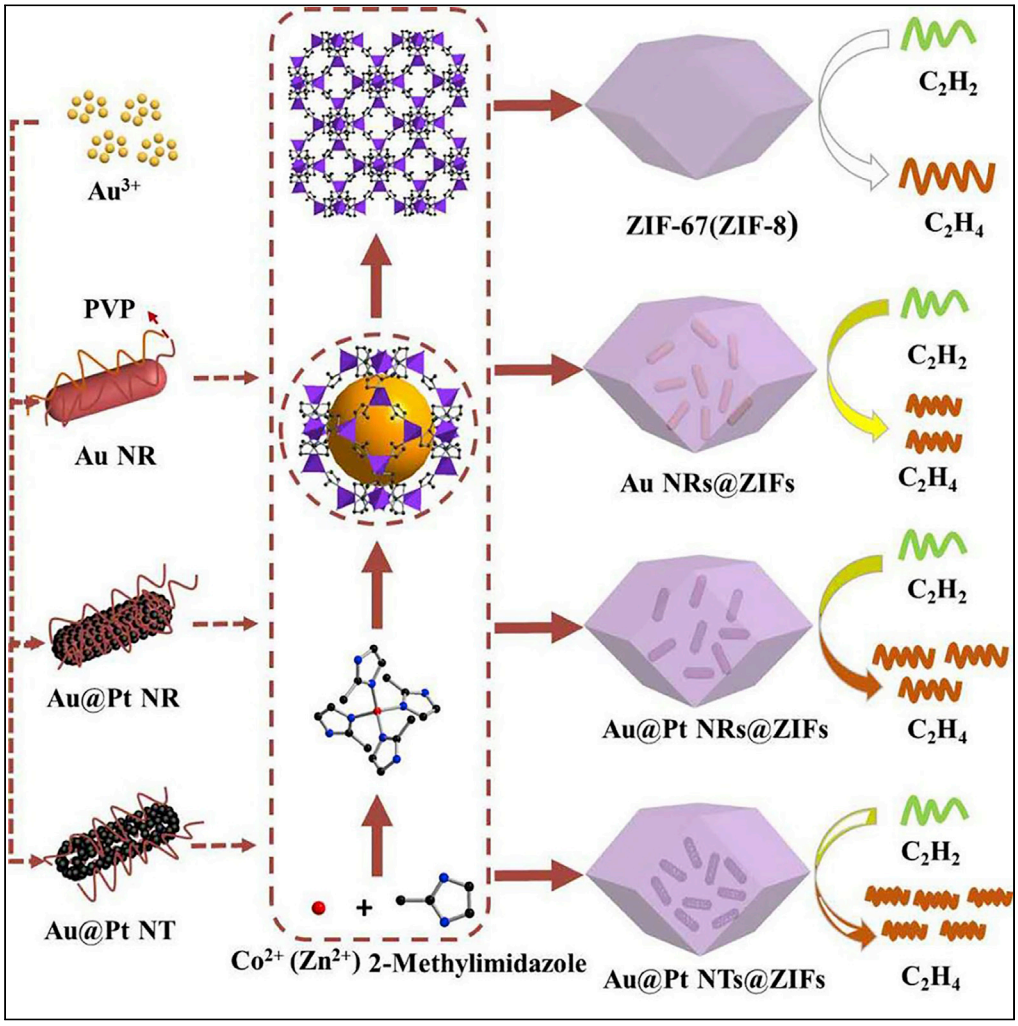

Jiajia Wang, Haitao Xu, Chengcheng Ao, ..., Lidong Zhang, Zhen-liang Xu, Yadong Li

xuhaitao@ecust.edu.cn (H.X.)
zhili@mail.tsinghua.edu.cn (Z.L.)
zld@ustc.edu.cn (L.Z.)

HIGHLIGHTS

Core-shell nanocomposite catalysts M@ZIFs are assembled

The M NRs and NTs are well dispersed and fully encapsulated in ZIF-67 and ZIF-8

$Au@Pt_{NT}$ enhance the selectivity and conversion for the semi-hydrogenation of acetylene

DFT calculations show $Au@Pt_{NT}$ has lower energy barrier compared with $Au@Pt_{NR}$

Wang et al., iScience 23, 101233
June 26, 2020
https://doi.org/10.1016/j.isci.2020.101233

iScience

CellPress
OPEN ACCESS

Article

Au@Pt Nanotubes within CoZn-Based Metal-Organic Framework for Highly Efficient Semi-hydrogenation of Acetylene

Jiajia Wang,[1,4] Haitao Xu,[1,5,*] Chengcheng Ao,[3,4] Xinbo Pan,[1,4] Xikuo Luo,[1] ShengJie Wei,[2] Zhi Li,[2,*] Lidong Zhang,[3,*] Zhen-liang Xu,[1] and Yadong Li[2]

SUMMARY

Designing nanocatalysts with synergetic functional component is a desirable strategy to achieve both high activity and selectivity for industrially important hydrogenation reaction. Herein, we fabricated a core-shell hollow Au@Pt NTs@ZIFs (ZIF, zeolitic imidazolate framework; NT, nanotube) nanocomposite as highly efficient catalysts for semi-hydrogenation of acetylene. Hollow Au@Pt NTs were synthesized by epitaxial growth of Pt shell on Au nanorods followed with oxidative etching of Au@Pt nanorod. The obtained hollow Au@Pt NTs were then homogeneously encapsulated within ZIFs through *in situ* crystallization. By combining the high activity of bimetallic nanotube and gas enrichment property of porous metal-organic frameworks, hollow Au@Pt NT@ZIF catalyst was demonstrated to show superior catalytic performance for the semi-hydrogenation of acetylene, in terms of both selectivity and activity, over those of monometallic Au and solid bimetal nanorod@ZIF counterparts. This catalysts design idea is believed to be inspirable for the development of highly efficient nanocomposite catalysts.

INTRODUCTION

Metal-organic frameworks (MOFs), constructed by the self-assembly of metal ions and organic linkers in an appropriate solvent (Altaf et al., 2018; Cook et al., 2013; Tsuruoka et al., 2018; Yaghi et al., 2003), have permanent microporous structures and are typically characterized by extraordinarily large surface areas, well-defined pore structures, and tailorable chemistries (Corma et al., 2010; Farrusseng et al., 2009; Feng et al., 2015; Lee et al., 2009; Zhang et al., 2018). These properties make MOFs potential candidates for various applications such as gas storage and separation (Alezi et al., 2015; Wang and Yuan, 2014; Furukawa et al., 2013; Suh et al., 2012), ion exchange (Gao et al., 2014), sensing (Li et al., 2018; Ma et al., 2012), drug delivery (Wu et al., 2014), and catalysis (Feng et al., 2012; Liu et al., 2014). In particular, the combination of functional guest species and MOFs can impart new functionalities owing to the guest-host synergistic effect (Dhakshinamoorthy and Garcia, 2012). Fabricating multicomponent nanostructures either by embedding nanoparticles (NPs) in MOF matrices (Jang et al., 2017; Zhao et al., 2018; Zlotea et al., 2010) or incorporating preformed NPs into MOFs (Buso et al., 2011; Lohe et al., 2011; Ma et al., 2018) is an efficient route for extending MOF applicability. In the latter case, preformed NPs with diverse sizes and structures can be encapsulated into MOFs to generate core-shell nanocomposites. Although a few researchers have successfully synthesized NP@MOF composites through constructing MOFs on the surface of functional NPs (Du et al., 2017; He et al., 2013; Shang et al., 2016; Sugikawa et al., 2013; Zhao et al., 2014), effective control over the dispersibility of NPs within the MOFs as well as the morphology and size of the shell materials remains significant challenges. For example, it is difficult to encapsulate NPs with random shapes and compositions owing to the competition between the homogeneous nucleation and the heterogeneous growth of MOFs on the NP surface. In the present work, we attempted to synthesize a core-shell nanocomposite, in which preformed NPs with well-defined morphologies were entirely confined within the MOF layers, as advanced nanocatalysts for selective hydrogenation of acetylene.

Ethylene is the basic raw material in the industrial manufacturing of polymers and fine chemicals. The catalytic semi-hydrogenation of acetylene, $C_2H_2 + H_2 \rightarrow C_2H_4$, is one of the most important reactions in the ethylene industry, since even trace amount of C_2H_2 in C_2H_4 can deactivate the downstream Ziegler-Natta catalyst for further polymerization. The main challenge of this reaction is to selectively hydrogenate acetylene into ethylene and meanwhile prevent the excess reduction of ethylene to ethane (Wang et al., 2019;

[1]School of Chemical Engineering, East China University of Science and Technology, Shanghai 200237, China

[2]Department of Chemistry, Tsinghua University, 100084 Beijing, China

[3]National Synchrotron Radiation Laboratory, University of Science and Technology of China, Hefei, Anhui 230029, P. R. China

[4]These authors contributed equally

[5]Lead Contact

*Correspondence: xuhaitao@ecust.edu.cn (H.X.), zhili@mail.tsinghua.edu.cn (Z.L.), zld@ustc.edu.cn (L.Z.)

https://doi.org/10.1016/j.isci.2020.101233

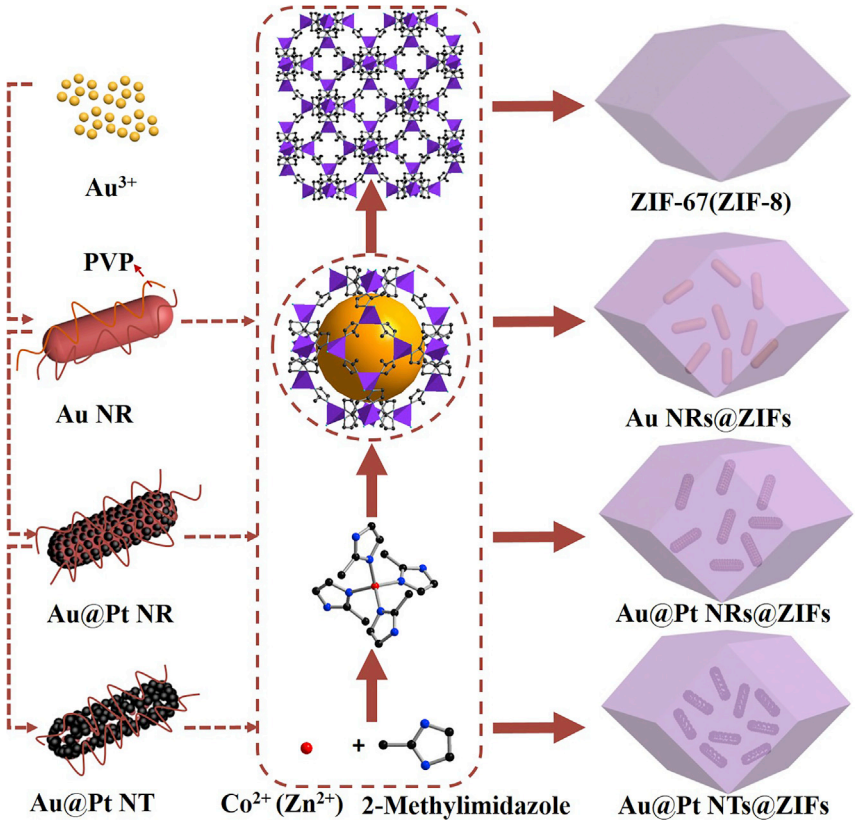

Figure 1. Schematic Illustration of the Formation of Au, Au@Pt NR, and Hollow Au@Pt NTs and Their ZIF Nanocomposites

Yang et al., 2015). In this process, metal NPs play a very important role in controlling the overall catalytic performance. Recently, Au nanomaterials have been found to be suitable catalysts for selective hydrogenation of acetylene (Sun et al., 2019). Apart from monometallic Au, bimetallic nanostructures have also attracted significant attention owing to their synergistic effects improving the physical and chemical properties of their monometallic counterpart (Yasukawa et al., 2012; Zhang et al., 2019). Given the enhanced properties of bimetallic nanostructures, controlling the synthesis of noble metal nanocrystals with well-defined morphology and size becomes very significant. Hollow Pt nanotubes (NTs) reportedly exhibited a much better catalytic activity than Au/Pt nanorods (NRs) and 5 nm Pt/C, which can be attributed to the unique tubular characteristic of the Pt nanostructure (Huang et al., 2016; Peng et al., 2010). However, Au NRs, Au@Pt NRs, and Au@Pt NTs were prone to agglomerate. A suitable carrier is important to maintain its morphology and dispersion for preventing its agglomeration and inactivation. Furthermore, inspired by the work wherein the encapsulation of Au NRs into porous MOFs led to enhanced stability and activity in applications such as catalysis or sensing (Chen et al., 2014; Zheng et al., 2016), we designed hollow Au@Pt NTs through etching interior Au of Au@Pt NRs and tried to encapsulate these NPs into zeolitic imidazolate framework (ZIF) nanocrystals in a core-shell-type configuration, forming NPs@ZIFs core-shell structures to maintain the morphology and dispersion of NPs and avoid agglomeration.

ZIFs were chosen as the host material owing to their porosity, high surface area, and relatively high structural robustness. The porous-robust ZIF-67 or ZIF-8 can be synthesized at mild temperature (room temperature), which is suitable for the supporter. Au NRs, Au@Pt NRs, and Au@Pt NTs were encapsulated into ZIFs forming well-dispersed NPs@ZIFs core-shell structures. Here, we report a facile and general encapsulation strategy to synthesize catalysts that incorporates different structures of NPs into ZIFs (Figure 1).

ZIF-67 is constructed by the assembly of cobalt ions and methyl imidazole. It has the same structure as that of ZIF-8, with sod topology, in which a large sod cage (11.6 Å) is accessible through a narrow six-ring pore (3.4 Å). By combining the catalytic properties of metal NPs with the large internal surface area, tunable

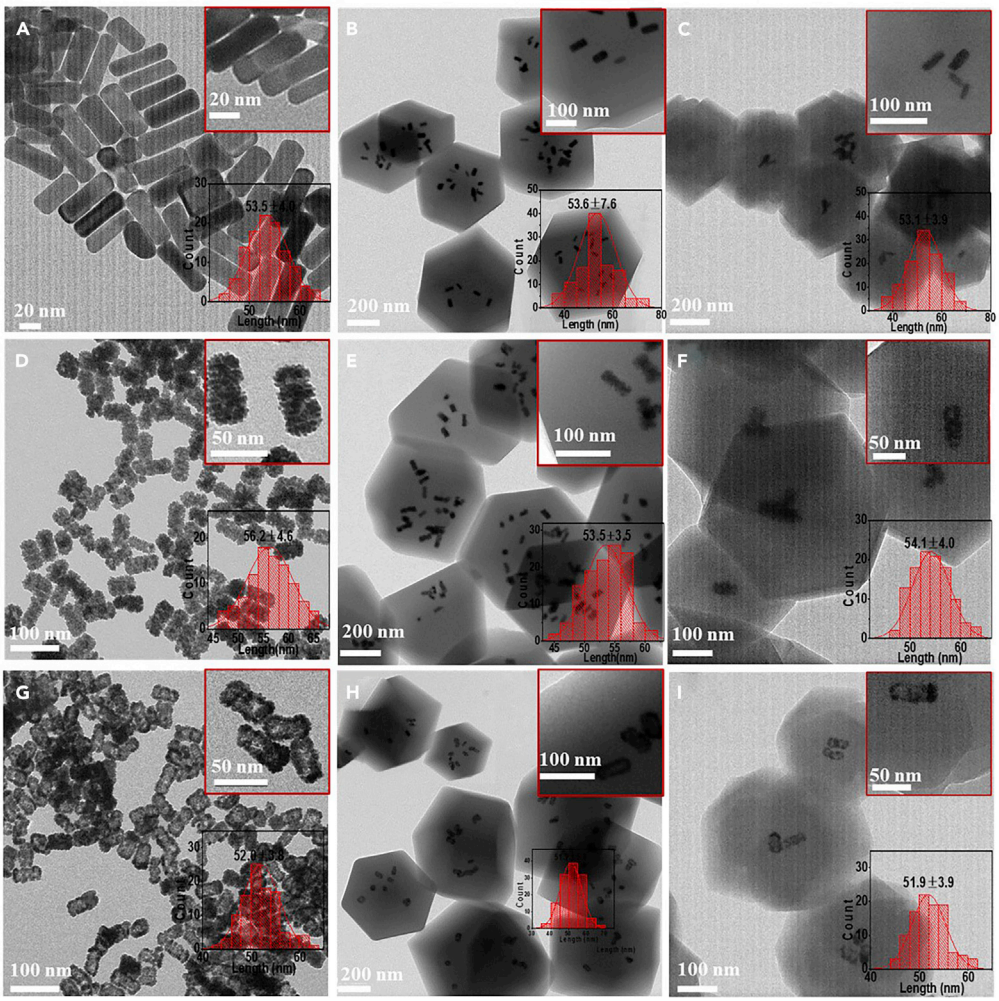

Figure 2. TEM Images of Different Samples

(A) Au NRs, (B) Au NRs@ZIF-67, (C) Au NRs@ZIF-8, (D) Au@Pt NRs, (E) Au@Pt NRs@ZIF-67, (F) Au@Pt NRs@ZIF-8, (G) Au@Pt NTs, (H) Au@Pt NTs@ZIF-67, and (I) Au@Pt NTs@ZIF-8.

crystal porosity, and unique chemical properties of ZIFs, the hydrogenation of acetylene was studied to elucidate the role of encapsulated nano-sized metal structures in catalytic activities.

RESULTS AND DISCUSSION

Au NRs with an average length of 53.5 nm (Figure 2A) were prepared by a previously reported procedure (Feng et al., 2008). Au@Pt NRs and hollow Au@Pt NTs were synthesized according to a previously reported method (Lee et al., 2016), with some modifications to obtain NPs with desired structures (Figures 2D and 2G). The lengths of Au@Pt NRs and hollow Au@Pt NTs were 56.2 and 52.0 nm, respectively. The surfaces of these NPs were functionalized with polyvinylpyrrolidone (PVP) after synthesis. The ZIF incorporation process was conducted with Au NRs, Au@Pt NRs and hollow Au@Pt NTs, respectively. In a typical procedure, cobalt nitrate hexahydrate (291 mg) and 2-methylimidazole (369.5 mg) were each dissolved in methanol (25 mL). Afterward, the ligand solution was poured into the pink solution containing Co^{2+} ions. After allowing the mixture to stand for 5 min, a PVP-Au@Pt NT solution, concentrated to 2 mL in methanol by centrifugation (12,000 rpm, 5 min), was injected into the above solution.

Thereafter, the resulting mixture was allowed to rest at room temperature for 24 h without mechanical perturbation. For this synthesis of NPs@ZIF-67 with well-defined morphology and size, the amount of PVP was a key factor. The encapsulation procedure is based on the successive adsorption of PVP-modified

NPs on the surface of the growing ZIF-67 crystals until the NPs are exhausted (Du et al., 2017). According to the investigation of the adsorption of amphiphilic PVP on solid surfaces, the polar and apolar groups in PVP are believed to promote the adsorption process (Mdluli et al., 2011). It can be seen that, without PVP, severe aggregation of Au@Pt NTs occurred during the preparation of the core-shell structure (Figure S13A). However, when excessive PVP was used in the synthesis, ZIF-67 rhombic dodecahedral shells of different sizes were observed, followed by agglomeration (Figure S13D), which can be attributed to the binding of PVP on the crystal surface. Thus, an appropriate amount of PVP is required to guarantee the surface functionalization of metal NPs and maintain the morphology of the MOFs. Scanning electron microscopy (SEM) images showed that Au@Pt NTs@ZIF-67 crystals with a uniform rhombic dodecahedral shape had a narrow size distribution with an average size of 767.9 nm (Figure S11). Transmission electron microscopy (TEM) images demonstrated that each ZIF-67 crystal contained multiple Au@Pt NTs that were fully confined within the MOF. Freestanding metal NTs were not observed (Figure 2H). The distance between the NTs varied from 10 to 450 nm, suggesting that Au@Pt NTs were well isolated from each other during the assembly process.

There were no remarkable deviations in the morphology and size among the encapsulated Au@Pt nanotubes. The size distribution of Au@Pt NTs@ZIF-67 nanocomposites ranged from 600 to 1,000 nm. To gain a better understanding of the formation of multi-core-shell structures, the encapsulation process was then investigated by conducting time-dependent experiments. Upon reacting for 30 min, the obtained products were spherical multi-Au@Pt NTs-ZIF-67 hybrids that possessed an average diameter of 600 nm. The spherical shells grew larger with an average size of 750 nm upon further extending the incubation time. After 8 h, the encapsulation process was nearly completed, and the hybrid spheres gradually evolved into rhombic dodecahedral shapes (Figure S14). The same strategy could be applied to encapsulate other nanostructured particles with different compositions (Figures 2B and 2E). Similarly, ZIF-8 can be selected as the host for embedding metal NPs. When Au@Pt nanotubes were used as seeds in the procedure, TEM revealed (Figure 2I) that the nanocomposites were of the same core-shell structure as Au@Pt NTs@ZIF-67, in which multiple Au@Pt nanotubes, ~51.9 nm in length, were coated with a ZIF-8 shell having a thickness of ~250 nm (Figure S12). The incorporated Au@Pt NTs maintained their integrity in the presence of a hollow interior, but the crystals were observed to be multilayered (Figure S12).

The crystal structure analysis of ZIF-67 and ZIF-8 composites from powder X-ray diffraction (XRD) patterns indicated that the incorporation of metal nanoparticles did not affect the crystalline structure of MOF. The two additional peaks originated from the presence of Au and Pt (Figures S16 and S17). Energy-dispersive X-ray spectroscopy (EDS) elemental mapping of Au@Pt NTs@ZIF-67 further revealed that Au and Pt were located only in the hollow Au@Pt nanotubes, whereas C and Co were homogeneously distributed throughout the entire nanoparticle assembly (Figure 3). The obvious double peaks in the elemental line scan along the radial direction also confirmed the hollow nanostructure feature of Au@Pt NTs, and the content of Pt was more than that of Au (Figure 3H). After these particles were exposed to the acetylene reduction reaction, their powder XRD patterns confirmed the stability of MOFs (Figure S19). The Brunauer-Emmett-Teller (BET) results showed that the surface areas of Au@Pt NTs@ZIF-67 and Au@Pt NTs@ZIF-8 were 1,543.6 and 888.5 m^2g^{-1}, respectively. These values are less than those of ZIF-67 and ZIF-8 possibly because the nanoparticles occupied a part of the micropores in the MOFs.

The hydrogenation reaction of acetylene, conducted in a fixed-bed reactor, was used as a probe reaction to compare the catalytic activities of these different samples.

Gas component concentrations were analyzed at specific times by gas chromatography (GC). The catalytic efficiencies of ZIFs, Au NRs@ZIFs, Au@Pt NRs@ZIFs, and Au@Pt NTs@ZIFs are summarized in Figure 4. At an operating temperature of 175°C, gas flowrate of 40 mL min^{-1}, and catalyst dosage of 50 mg, the acetylene conversion was 12.9% for Au NRs@ZIF-67, 43.5% for Au@Pt NRs@ZIF-67, and 69.1% for Au@Pt NTs@ZIF-67; and ethylene yields were 9.1% for Au NRs@ZIF-67, 35.1% for Au@Pt NRs@ZIF-67, and 49.3% for Au@Pt NTs@ZIF-67, respectively. The above results reveal that Au@Pt NRs@ZIF-67 showed better catalytic performance than Au NRs@ZIF-67, which can be ascribed to the highly active Pt nanoparticles loaded on the Au NRs. More interestingly, hollow Au@Pt NTs@ZIF-67 exhibited the best catalytic activity with slightly compromised selectivity, owing to the unique tubular structure that allowed the existence of more active sites on the surface of the Au@Pt nanotube wall. Comparing the conversion of the catalysts with different nanoparticles, the bimetallic Au@Pt NTs or Au@Pt NRs in ZIFs greatly facilitated the reaction of

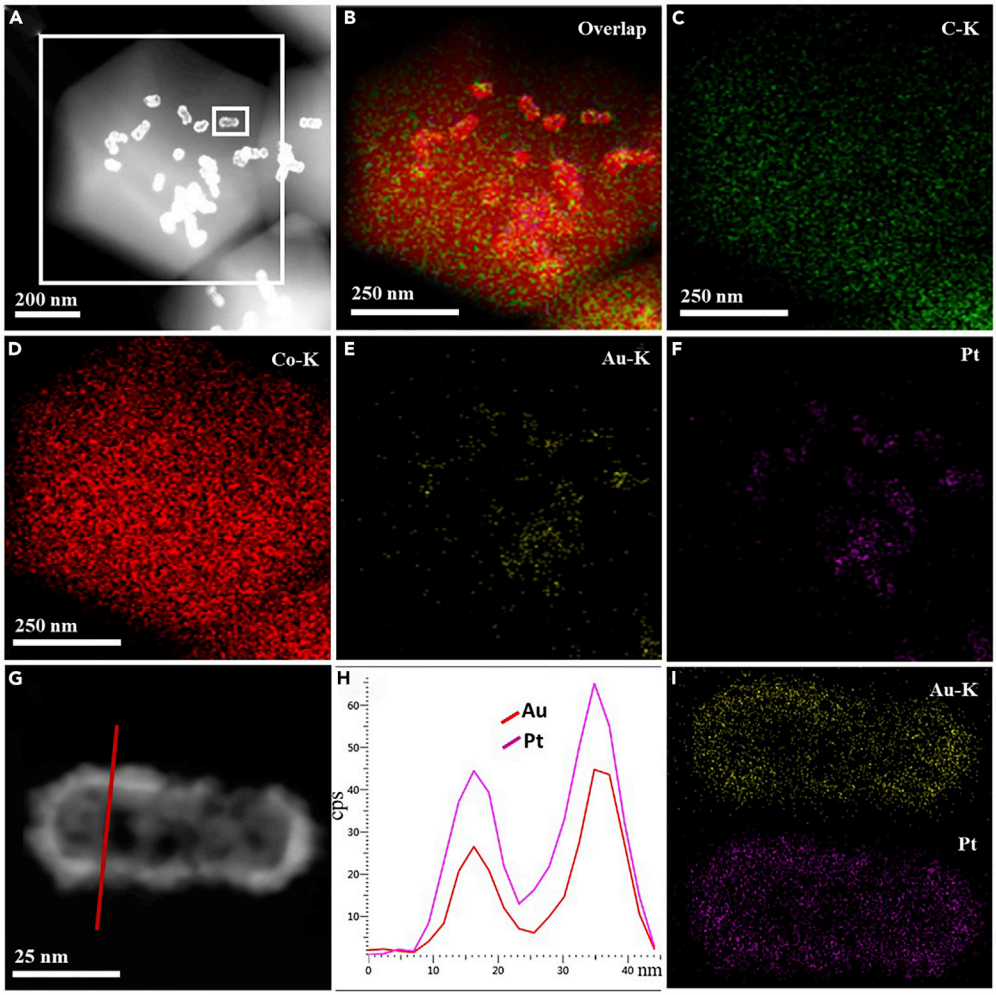

Figure 3. High-Angle Annular Dark-Field Scanning TEM Images and EDS Elemental Mapping Images

High-angle annular dark-field scanning TEM images of (A) Au@Pt NTs@ZIF-67 and (G) Au@Pt NTs. EDS elemental mapping of (B–F) Au@Pt NTs@ZIF-67 marked in (A) and (I) Au@Pt NT marked in (A). EDS line scan of (H) Au@Pt NTs.

semi-hydrogenation of acetylene than monometallic Au NRs. The existence of highly active Pt around Au promotes the conversion of C_2H_2 hydrogenation to C_2H_4 owing to the synergistic effects of bimetallic nanostructures. The reaction was then studied over Au NRs@ZIF-8, Au@Pt NRs@ZIF-8, and Au@Pt NTs@ZIF-8. Results similar to those for NPs@ZIF-67 were obtained. Au@Pt NTs@ZIF-8 showed the best catalytic performance with 88.1% conversion at 175°C. Compared with the Au@Pt NTs@ZIF-67 catalyst, acetylene conversion can be further improved by using ZIF-8 as the host material. After catalysis, Au@Pt nanotubes in the core maintained their tubular features, and the particles retained their original morphologies, and the morphology of the Au@Pt NTs encapsulated in ZIFs was well dispersed, showing the core-shell structure was intact and not damaged, albeit with a roughened surface (Figure S15), suggesting their robust structural stability so that their activities would not decrease and the catalyst could be reused. Compared with other similar catalysts reported for the acetylene semi-hydrogenation reaction, these M@ZIFs catalysts exhibited higher acetylene conversion or ethylene selectivity at a lower temperature (Gonçalves et al., 2020; Osswald et al., 2008; Redfern et al., 2018; Shun et al., 2015; Yang et al., 2015); the catalytic effects of this work and other similar materials have been listed in Table S2. Obviously, some catalysts showed high acetylene conversion but low ethylene selectivity, whereas some catalysts showed high ethylene selectivity but low acetylene conversion. In terms of both selectivity and activity, the catalysts Au@Pt NTs@ZIF-67 and Au@Pt NTs@ZIF-8 were better than that of the other catalysts, showing their superior catalytic performance for the semi-hydrogenation of acetylene. Encapsulation of

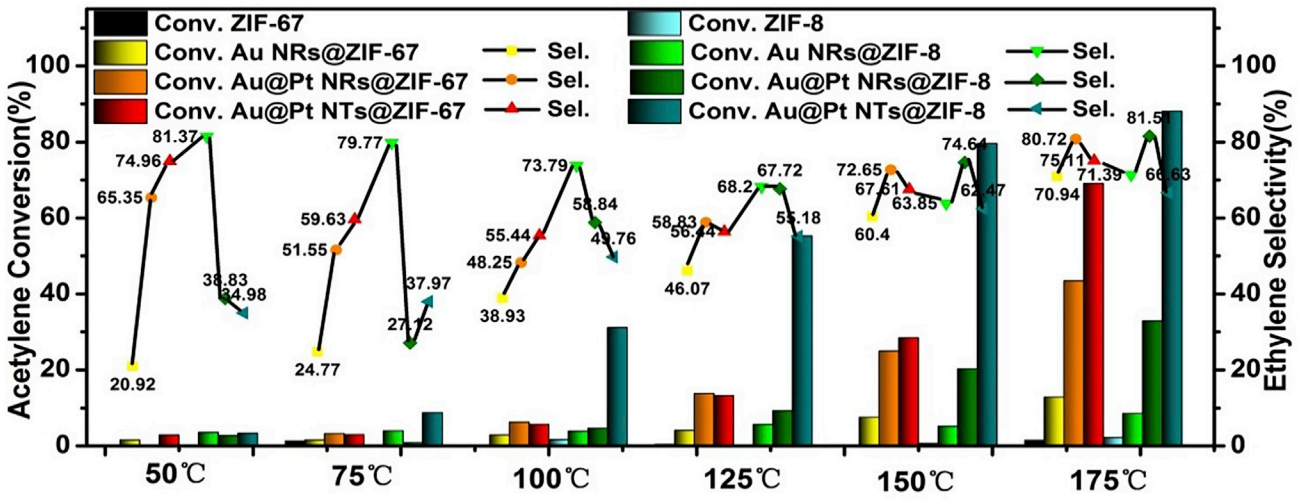

Figure 4. Acetylene Conversion and Ethylene Selectivity Over the Catalysts NPs@ZIF-67 and NPs@ZIF-8

hollow metal NTs with excellent catalytic properties imparts functionality to the porous MOFs, leading to an even higher catalytic activity for the semi-hydrogenation reaction of acetylene.

To further explain the results, theoretical insights were explored by DFT calculations (Figure 5). Based on the aforementioned catalysts analyzed, models of Au@Pt NTs and Au@Pt NRs have been constructed in Figures 5 and S22. TS of each step of C_2H_2 hydrogenation to C_2H_4 on previous constructed configuration was searched by Dimer method. And energetics of forming C_2H_3* (* represents adsorbate) and C_2H_4* on two catalysts were shown in Figures S23 and S24. Energy barriers of C_2H_2* converted to C_2H_3* and then to C_2H_4* on Au@Pt NTs is 0.85 and 0.64 eV, respectively. For catalyst Au@Pt NRs, energy barriers of two steps are 0.65 and 1.10 eV. Thus, the highest energy barriers of Au@Pt NTs and Au@Pt NRs are 0.85 and 1.10 eV. Obviously, Au@Pt NTs have a lower energy barrier compared with Au@Pt NRs, which suggests that Au@Pt NRs are favorable in thermodynamics. This result is consistent with experimental analysis.

Conclusions

In summary, multifunctional nanocatalysts, Au@Pt NTs@ZIFs for which multiple hollow Au@Pt NTs are fully incorporated in the ZIFs (ZIF-67 and ZIF-8) matrix, can be successfully assembled by a facile *in situ* encapsulation strategy. To the best of our knowledge, this is the first report on a synthesis of multicore-shell nanoparticles with hollow Au@Pt NTs as cores. This synthesis strategy allows the encapsulation of hollow metal nanotubes in a non-aggregated pattern and the fabrication of size-controlled MOFs by adjusting the amount of added ligand. In combination with the unique tubular structure of hollow Au@Pt NTs and porosity of ZIFs, the as-prepared Au@Pt NTs@ZIFs exhibited high catalytic performance and ethylene selectivity in the semi-hydrogenation of acetylene. We believe this nanocomposite encapsulation design, which involves the trapping of hollow bimetallic NPs in MOFs, will promote their potential applications in catalysis.

Limitations of the Study

This study provides a strategy for encapsulating metal nanotubes into ZIFs to form multifunctional composite materials. However, the multi-step synthesis of Au@Pt NTs and Au@Pt NTs@ZIFs makes the material costly. Limited by the cost, it is currently difficult to achieve industrialization. Hence, a simpler and cheaper method for preparing multifunctional composites should be developed in future research.

Resource Availability

Lead Contact

Further information and requests for resources and reagents should be directed to and will be fulfilled by the Lead Contact, Haitao Xu (xuhaitao@ecust.edu.cn).

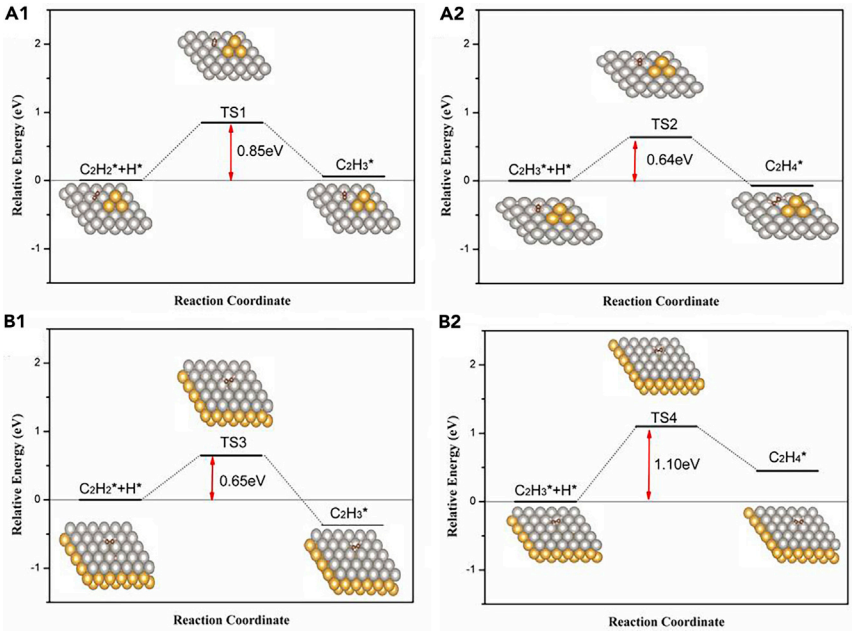

Figure 5. DFT Calculations for Energetics Diagram of C2H2 Hydrogenation to C2H4

Energetics diagram of C_2H_2 hydrogenation to C_2H_4 (A1) and (A2) for Au@Pt NTs and (B1) and (B2) for Au@Pt NRs. Brown is carbon atom, white is hydrogen, orange is gold, and gray is platinum.

Materials Availability

This study did not generate new unique reagents.

Data and Code Availability

The published article includes all datasets/code generated or analyzed during this study.

METHODS

All methods can be found in the accompanying Transparent Methods supplemental file.

SUPPLEMENTAL INFORMATION

Supplemental Information can be found online at https://doi.org/10.1016/j.isci.2020.101233.

ACKNOWLEDGMENTS

We thank Prof. Rong Huang, Prof. Ruijuan Qi from Key Laboratory of Polar Materials and Devices Ministry of Education East China Normal University for HAADF-STEM measurements, and Ms. Lihui Zhou at Research Center of Analysis and Test of East China University of Science and Technology for the help on TEM analysis. We gratefully acknowledge the financial support from the National Natural Science Foundation of China (No. 21371058, 21890383) and the National Key R&D Program of China (2018YFA0702003).

AUTHOR CONTRIBUTIONS

J.W. and X.P. completed most of the experiments, analyzed the data, and wrote the paper. C.A. completed the DFT calculation. X.L. helped with the materials synthesis. S.W. completed the experiment of acetylene hydrogenation. H.X. conceived the experimental scheme and wrote the paper. Z.L. and Y.L. discussed the results and wrote the article. L.Z. provided the resource for DFT calculations and wrote the calculation part of the manuscript. Z.X. discussed the results and commented on the manuscript. All the authors have given approval to the final version of the manuscript.

DECLARATION OF INTERESTS

The authors declare no competing interest.

Received: March 14, 2020
Revised: April 30, 2020
Accepted: June 1, 2020
Published: June 26, 2020

REFERENCES

Alezi, D., Belmabkhout, Y., Suetin, M., Bhatt, P., Weselinski, L., Solovyeva, V., Adil, K., Spanopoulos, I., Trikalitis, P., Emwas, A., and Eddaoudi, M. (2015). MOF crystal chemistry paving the way to gas storage needs: aluminum-based soc-MOF for CH_4, O_2, and CO_2 storage. J. Am. Chem. Soc. *137*, 13308–13318.

Altaf, M., Sohail, M., Mansha, M., Iqbal, N., Sher, M., Fazal, A., Ullah, N., and Isab, A. (2018). Synthesis, characterization, and photoelectrochemical catalytic studies of a water-stable zinc-based metal–organic framework. Chemsuschem *11*, 542–546.

Buso, D., Nairn, K.M., Gimona, M., Hill, A.J., and Falcaro, P. (2011). Fast synthesis of MOF-5 microcrystals using Sol–Gel SiO_2 nanoparticles. Chem. Mater. *23*, 929–934.

Chen, L., Peng, Y., Wang, H., Gu, Z., and Duan, C. (2014). Synthesis of Au@ZIF-8 single- or multi-core-shell structures for photocatalysis. Chem. Commun. (Camb.) *50*, 8651–8654.

Cook, T.R., Zheng, Y.R., and Stang, P.J. (2013). Metal-organic frameworks and self-assembled supramolecular coordination complexes: comparing and contrasting the design, synthesis and functionality of metal-organic materials. Cheminform *113*, 734–777.

Corma, A., Garcia, H., and Llabrés i Xamena, F.X. (2010). Engineering metal organic frameworks for heterogeneous catalysis. Chem. Rev. *110*, 4606–4655.

Dhakshinamoorthy, A., and Garcia, H. (2012). Catalysis by metal nanoparticles embedded on metal-organic frameworks. Chem. Soc. Rev. *41*, 5262–5284.

Du, N., Wang, C., Long, R., and Xiong, Y. (2017). N-doped carbon-stabilized PtCo nanoparticles derived from Pt@ZIF-67: highly active and durable catalysts for oxygen reduction reaction. Nano Res. *10*, 3228–3237.

Farrusseng, D., Aguado, S., and Pinel, C. (2009). Metal–organic frameworks: opportunities for catalysis. Angew. Chem. Int. Ed. *48*, 7502–7513.

Feng, D., Gu, Z., Li, J., Jiang, H., Wei, Z., and Zhou, H. (2012). Zirconium-metalloporphyrin PCN-222: mesoporous metal–organic frameworks with ultrahigh stability as biomimetic catalysts. Angew. Chem. Int. Ed. *51*, 10307–10310.

Feng, D., Liu, T., Su, J., Bosch, M., Wei, Z., Wan, W., Yuan, D., Chen, Y., Wang, X., Wang, K., et al. (2015). Stable metal-organic frameworks containing single-molecule traps for enzyme encapsulation. Nat. Commun. *6*, 5979.

Feng, L., Wu, X., Ren, L., Xiang, Y., He, W., Zhang, K., Zhou, W., and Xie, S. (2008). Well-controlled synthesis of Au@Pt nanostructures by gold-nanorod-seeded growth. Chemistry *14*, 9764–9771.

Furukawa, H., Cordova, K.E., O'Keeffe, M., and Yaghi, O.M. (2013). The chemistry and applications of metal-organic frameworks. Science *341*, 1230444.

Gao, L., Li, C.Y., Chan, K.Y., and Chen, Z.N. (2014). Metal-organic framework threaded with aminated polymer formed in situ for fast and reversible ion exchange. J. Am. Chem. Soc. *136*, 7209–7212.

Gonçalves, L.P.L., Wang, J., Vinati, S., Barborini, E., Wei, X.-K., Heggen, M., Franco, M., Sousa, J.P.S., Petrovykh, D.Y., Soares, O.S.G.P., et al. (2020). Combined experimental and theoretical study of acetylene semi-hydrogenation over Pd/Al_2O_3. Int. J. Hydrogen Energ. *45*, 1283–1296.

He, L., Liu, Y., Liu, J., Xiong, Y., Zheng, J., Liu, Y., and Tang, Z. (2013). Core-shell noble-Metal@Metal-organic-framework nanoparticles with highly selective sensing property. Angew. Chem. Int. Ed. *52*, 3741–3745.

Huang, Z., Raciti, D., Yu, S., Zhang, L., Deng, L., He, J., Liu, Y., Khashab, N., Wang, C., Long, J., and Nie, Z. (2016). Synthesis of platinum nanotubes and nanorings via simultaneous metal alloying and etching. J. Am. Chem. Soc. *138*, 6332–6335.

Jang, J., Koo, W., Choi, S.J., and Kim, I. (2017). Metal organic framework-templated chemiresistor: sensing type transition from p-to-n using hollow metal oxide polyhedron via galvanic replacement. J. Am. Chem. Soc. *139*, 11868–11876.

Lee, J.Y., Farha, O.K., Roberts, J., Scheidt, K.A., Nguyen, S.B.T., and Hupp, J.T. (2009). Metal–organic framework materials as catalysts. Chem. Soc. Rev. *38*, 1450–1459.

Lee, S., Jang, H.J., Jang, H.Y., Hong, S., Moh, S.H., and Park, S. (2016). Synthesis and optical property characterization of elongated AuPt and Pt@Au metal nanoframes. Nanoscale *8*, 4491–4494.

Li, Q., Xue, D.X., Zhang, Y.F., Zhang, Z.H., and Gao, Z. (2018). Syntheses, crystal structures and photoluminescence properties of five Cd/Zn–organic frameworks. J. Mol. Struct. *1164*, 123–128.

Liu, J., Chen, L., Cui, H., Zhang, J., Zhang, L., and Su, C. (2014). Applications of metal-organic frameworks in heterogeneous supramolecular catalysis. Chem. Soc. Rev. *43*, 6011–6061.

Lohe, M., Gedrich, K., Freudenberg, T., Kockrick, E., Dellmann, T., and Kaskel, S. (2011). Heating and separation using nanomagnet-functionalized metal-organic frameworks. Chem. Commun. (Camb.) *47*, 3075–3077.

Ma, J.-P., Yu, Y., and Dong, Y.-B. (2012). Fluorene-based Cu(ii)-MOF: a visual colorimetric anion sensor and separator based on an anion-exchange approach. Chem. Commun. (Camb.) *48*, 2946–2948.

Ma, R., Yang, P., Ma, Y., and Bian, F. (2018). Facile synthesis of magnetic hierarchical core-shell structured Fe_3O_4@PDA-Pd@MOF nanocomposites: highly integrated multifunctional catalysts. Chemcatchem *10*, 1446–1454.

Mdluli, P.S., Sosibo, N.M., Mashazi, P.N., Nyokong, T., Tshikhudo, R.T., Skepu, A., and Lingen, E. (2011). Selective adsorption of PVP on the surface of silver nanoparticles: a molecular dynamics study. J. Mol. Struct. *1004*, 131–137.

Osswald, J., Kovnir, K., Armbruster, M., Giedigkeit, R., Jentoft, R.E., Wild, U., Grin, Y., and Schlogl, R. (2008). Palladium–gallium intermetallic compounds for the selective hydrogenation of acetylene Part II: surface characterization and catalytic performance. J. Catal. *258*, 219–227.

Peng, Z., Wu, J., and Yang, H. (2010). Synthesis and oxygen reduction electrocatalytic property of platinum hollow and platinum-on-silver nanoparticles†. Chem. Mater. *22*, 1098–1106.

Redfern, L.R., Zhanyong, L., Xuan, Z., and Farha, O.K. (2018). Highly selective acetylene semihydrogenation catalyzed by Cu nanoparticles supported in a metal–organic framework. ACS Appl. Nano Mater. *1*, 4413–4417.

Shang, W., Zeng, C., Du, Y., Hui, H., Liang, X., Chi, C., Wang, K., Wang, Z., and Tian, J. (2016). Core-shell gold Nanorod@Metal-organic framework nanoprobes for multimodality diagnosis of Glioma. Adv. Mater. *29*, 1604381–1604389.

Shun, Z., Chen, C., Jang, B.W.-L., and Zhu, A. (2015). Radio-frequency H_2 plasma treatment of AuPd/TiO_2 catalyst for selective hydrogenation of acetylene in excess ethylene. Catal. Today *256*, 161–169.

Sugikawa, K., Nagata, S., Furukawa, Y., Kokado, K., and Sada, K. (2013). Stable and functional gold nanorod composites with a metal–organic framework crystalline shell. Chem. Mater. *25*, 2565–2570.

Suh, M.P., Park, H.J., Prasad, T.K., and Lim, D.W. (2012). Hydrogen storage in metal-organic frameworks. Chem. Rev. *112*, 782–835.

Sun, X., Li, F., Shi, J., Zheng, Y., Su, H., Sun, L., Peng, S., and Qi, C. (2019). Gold nanoparticles supported on MgOx-Al_2O_3 composite oxide: an efficient catalyst for selective hydrogenation of acetylene. Appl. Surf. Sci. *487*, 625–633.

Tsuruoka, T., Inoue, K., Miyanaga, A., Tobiishi, K., Ohhashi, T., Hata, M., Takashima, Y., and Akamatsu, K. (2018). Crystal conversion between metal-organic frameworks with different crystal topologies for efficient crystal design on two-dimensional substrates. J. Cryst. Growth *487*, 1–7.

Wang, W., and Yuan, D. (2014). Mesoporous carbon originated from non-permanent porous MOFs for gas storage and CO_2/CH_4 separation. Sci. Rep. *4*, 5711.

Wang, L., Li, F., Chen, Y., and Chen, J. (2019). Selective hydrogenation of acetylene on SiO_2-supported Ni-Ga alloy and intermetallic compoun. J. Energy Chem. *29*, 48–57.

Wu, Y.N., Zhou, M., Li, S., Li, Z., and Guan, X. (2014). Magnetic metal–organic frameworks: γ-Fe_2O_3@MOFs via confined in situ pyrolysis method for drug delivery. Small *10*, 2927–2936.

Yaghi, O.M., O'Keeffe, M., Ockwig, N.W., Chae, H.K., Eddaoudi, M., and Kim, J. (2003). Reticular synthesis and the design of new materials. Nature *423*, 705–714.

Yang, J., Zhang, F., Lu, H., Hong, X., Jiang, H., Wu, Y., and Li, Y. (2015). Hollow Zn/Co ZIF particles derived from core–shell ZIF-67@ZIF-8 as selective catalyst for the semi-hydrogenation of acetylene. Angew. Chem. Int. Ed. *54*, 10889–10893.

Yasukawa, T., Miyamura, H., and Kobayashi, S. (2012). Polymer-incarcerated chiral Rh/Ag nanoparticles for asymmetric 1,4-addition reactions of arylboronic acids to enones: remarkable effects of bimetallic structure on activity and metal leaching. J. Am. Chem. Soc. *134*, 16963–16966.

Zhang, R., Zhou, T., Wang, L., and Zhang, T. (2018). Metal−Organic frameworks (MOFs) derived hierarchical Co_3O_4 structures as efficient sensing materials for acetone detection. ACS Appl. Mater. Interfaces *10*, 9765.

Zhang, T., Xing, Y., Song, Y., Gu, Y., Yan, X., Lu, N., Liu, H., Xu, Z., Xu, H., Zhang, Z., and Yang, M. (2019). AuPt/MOF-Graphene: a synergistic catalyst with surprisingly high peroxidase-like activity and its application for H_2O_2 detection. Anal. Chem. *91*, 10589–10595.

Zhao, M., Deng, K., He, L., Liu, Y., Li, G., Zhao, H., and Tang, Z. (2014). Core-shell palladium Nanoparticle@Metal-organic frameworks as multifunctional catalysts for cascade reactions. J. Am. Chem. Soc. *136*, 1738–1741.

Zhao, X., Xu, H., Wang, X., Zheng, Z., Xu, Z., and Ge, J. (2018). Monodisperse metal–organic framework nanospheres with encapsulated core–shell nanoparticles Pt/Au@Pd@{Co_2(oba)$_4$(3-bpdh)$_2$4H_2O for the highly selective conversion of CO_2 to CO. ACS Appl. Mater. Interfaces *10*, 15096–15103.

Zheng, G., de Marchi, S., López-Puente, V., Sentosun, K., Polavarapu, L., Pérez-Juste, I., Hill, E.H., Bals, S., Liz-Marzán, L.M., Pastoriza-Santos, I., and Pérez-Juste, J. (2016). Encapsulation of single plasmonic nanoparticles within ZIF-8 and SERS analysis of the MOF flexibility. Small *12*, 3935–3943.

Zlotea, C., Campesi, R., Cuevas, F., Leroy, E., Dibandjo, P., Volkringer, C., Loiseau, T., Férey, G., and Latroche, M. (2010). Pd nanoparticles embedded into a metal-organic framework: synthesis, structural characteristics, and hydrogen sorption properties. J. Am. Chem. Soc. *132*, 2991–2997.

iScience, Volume *23*

Supplemental Information

Au@Pt Nanotubes within CoZn-Based Metal-Organic Framework for Highly Efficient Semi-hydrogenation of Acetylene

Jiajia Wang, Haitao Xu, Chengcheng Ao, Xinbo Pan, Xikuo Luo, ShengJie Wei, Zhi Li, Lidong Zhang, Zhen-liang Xu, and Yadong Li

Supplementary Information

CONTENT:

1. Transparent Method

All the chemicals were used without further purification. Trichlorogold hydrate hydrochloride ($HAuCl_4 \cdot 4H_2O$, 99.9%), chloroplatinic acid hexahydrate ($H_2PtCl_6\ 6H_2O$), L-ascorbic acid (AA, $C_6H_8O_6$, ≥99%), silver nitrate ($AgNO_3$, >99%), cetyltrimethylammonium bromide (CTAB, $C_{19}H_{42}BrN$, ≥99%) were purchased from Sinopharm Chemical Reagent company. Sodium tetrahydroborate ($NaBH_4$, ≥96%) was purchased from Shanghai Tianlian Chemical Technology. Sodium iodide (NaI, 99.5%) was provided by Macklin. Sulphuric acid (H_2SO_4, 95%-98%) and methanol (99.5%) were purchased from Titan. Cobaltous Nitrate Hexahydrate (99%) and 2-Methylimidazole (99%) were purchased from Acros, zinc nitrate hexahydrate was purchased from Alfa Aesar. Powder X-ray diffraction (PXRD) data were collected on a Bruker AXS RINT 2000 Rigaku and recorded in the 2θ range of 5-80 º. Transmission electron microscopy (TEM) was carried out using JEM-1400 at 200 kV and high-resolution TEM imaging was carried out using JEM-2100. High angle annular dark field scanning transmission electron microscopy (HAADF-STEM) imaging and energy-dispersive X-ray spectroscopy (EDS) elemental mapping were carried out on JEM-2100 at 200 kV. Scanning electron microscopy (SEM) measurement was performed on a Phenom ProX field emission scanning electron microscope. Nitrogen adsorption-desorption measurements were conducted at 77K on a surface area and pore size analyzer (JK-122F) after the samples were degassed at 120 ℃ for 2 h. The specific surface area and the pore size distribution were calculated using the Brunauer-Emmett-Teller (BET) and Barrett-Joyner-Halenda (BJH) methods, respectively. In addition, the former was estimated using adsorption data in the relative pressure (P/P_0) range of 0.05-0.3. The noble metal content in different samples was determined by inductively coupled plasma mass spectrometer (ICP-MS, Thermo Fisher Scientific). TGA experiments were performed on Perkin-Elmer TGA analyzer heated from room temperature to 1000℃ under nitrogen gas with a heating rate of 8℃/min under N_2 atmosphere. The noble metal content was analyzed Agilent 725 ICP-OES. The hydrogenation of acetylene: 50 mg catalyst was loaded in a microreactor with a diameter of 6 mm. The catalyst was activated at 150℃ for 3 h with hydrogen. Acetylene (0.5%) was hydrogenated in admixture with ethylene (50%) and hydrogen (5%) over the catalyst. Aliquots were taken at specific time for determination of component concentrations by GC. Conversion and se-

lectivity were calculated as: Conversion= (C_{feed}-C_x) / C_{feed}, Selectivity= (C_{feed}-C_x) / (C_{feed}-C_x+C_{ethane}+2C_{C4Hx}); Where C_{feed} represents the acetylene concentration in the feed, C_x is the acetylene concentration in the product, C_{ethane} and C_{C4Hx} are the amounts of formed ethane and C4 hydrocarbons, respectively. For calculating the selectivity, it is assumed that acetylene is only hydrogenated to ethylene, which may be further hydrogenated to ethane. The selectivity towards C4 hydrocarbons is calculated following the same scheme. Higher hydrocarbons than C4 were not observed in the experiments and the carbon balance was between 99-100 %. All spin-polarized DFT calculations were performed by Vienna ab initio Simulation Packages (VASP) implemented with the exchange-correlation functional Perdew-Burke-Ernzerhof (PBE), one of generalized gradient approximation (GGA). And projector augmented wave (PAW) with a cut-off energy of 500 eV was adopted to described the interactions between the atomic cores and electrons. The model was constructed based on Pt (1 1 1) and Au (1 1 1) 4 × 4 × 1unit cells with all atoms full relaxed. The vacuum layers of 15 Å was set along *z*-xis to avoid neighboring image interactions. The Gamma 3 × 3 × 1 *k*-points grid was sampled in Brillouin zone. Meantime，Grimme's scheme (DFT-D2) was adopted as van der Waals interactions. Energy barrier of each step was calculated through search transition states (TS) using Dimer method. Then the TS was confirmed by vibrational frequency analyze which has only one imaginary frequency.

2. Synthetic procedures

Synthesis of Au NRs using a seed-mediated growth procedure: A seed solution was first prepared as follows: CTAB (7.5 mL, 0.1M) was mixed with $HAuCl_4$ (100 μL, 24.28 mM), the mixture was diluted to 9.4 mL, and stirred with a magnetic stirrer. Then, ice-cold $NaBH_4$ (0.6 mL,0.01M) was added. The solution color immediately turned from bright yellow to brown, indicating the formation of good seeds. The seeds were used within 2–5 h.

The growth solution was prepared in a 100 ml conical flask. CTAB (100 mL, 0.1M) was mixed with $HAuCl_4$ (2 mL, 24.28 mM), H_2SO_4 (2 mL, 0.5M), $AgNO_3$ (1 mL, 10 mM), and AA (0.8 mL, 0.1M). Then the seed solution (240 μL) was added to the above growth solution to initiate the growth of the Au NRs. After 12 h, the reaction was stopped. The obtained Au nanorods were purified by centrifuging the solution at 12000 rpm for 5 min. The precipitation was redispersed in 10 mL deionized water.

Synthesis of Au@Pt NRs: 4 mL of 50 mM CTAB, 1 mL of Au NRs, 2.14 mL H_2O, 140 μL of 2 mM $AgNO_3$, and 780 μL of 0.1 M AA were added to a vial in the presence of iodide ions (50 μM). The solution was heated to 70° C and kept in an oil bath to promote the deposition of Ag layers onto the Au NRs. After 1 h, 1940 μL of 2 mM H_2PtCl_6 solution were injected into the solution. The mixture was kept at 70° C for approximately 3 h. After completion of the reaction, the Au@Pt NRs were separated from the solution by centrifugation (12000 rpm, 5 min). The precipitates were redispersed in 1 mL deionized water.

Synthesis of Au@Pt NTs: 4 mL of 50 mM CTAB, 1 mL of Au@Pt NRs, 2.57 mL H_2O, 2.43 mL of 1 mM $HAuCl_4$ were added to a vial in the presence of iodide ions (50 μM). Then, the vial left in 50 ° C oil bath for 1 h. After the reaction, the AuPt NTs were separated from the solution by centrifugation (12000 rpm, 5 min). The precipitates were redispersed in 1 mL deionized water.

Preparation of PVP modified Au NRs, Au@Pt NRs and hollow AuPt nanostructures: 5 mL Au NRs solution was added to a solution of PVP (0.2g, Mw=58000) in water (15 mL), and the mixture was stirred for 24 h at room temperature. CTAB on Au NRs was

exchanged by PVP molecules to form PVP-Au NRs. Au@Pt NRs and hollow AuPt nanostructures were modified with PVP molecules using the same procedure.

Synthesis of ZIF-67 and ZIF-8: 291 mg of cobalt nitrate hexahydrate and 369.5 mg of 2-methylimidazole were each dissolved in 25 mL methanol. The latter ligand solution was poured into the former pink solution. After 24 h, a purple solid was collected by centrifugation (5000 rpm, 3 min), washed with methanol three times and dried at room temperature.

297.5 mg of zinc nitrate hexahydrate and 82.1 mg of 2-methylimidazole were each dissolved in 25 mL methanol. The latter ligand solution was poured into the former solution. After 24 h, a white solid was collected by centrifugation (5000 rpm, 3 min), washed with methanol three times and dried at room temperature.

Synthesis of Au NRs@ZIF-67, Au@Pt NRs@ZIF-67 and Au@Pt NTs@ZIF-67: 2-methylimidazol solution (369.5 mg in 25 mL methanol) was added one shot to $Co(NO_3)_2$ $6H_2O$ solution (291 mg in 25 mL methanol). Being kept still for 5 min, A PVP-Au NRs solution (8 mL) concentrated to 2 mL in methanol by centrifugation (12000 rpm, 5 min) was injected into the above mixed solution. After 24 h, the obtained violet precipitate was collected by centrifugation (5000 rpm, 3 min), washed with methanol three times and dried at room temperature for 48 h. The same strategy could be applied to encapsulate Au@Pt NRs and Au@Pt NTs.

Synthesis of Au NRs@ZIF-8, Au@Pt NRs@ZIF-8 and Au@Pt NTs@ZIF-8: 2-methylimidazol solution (82.1 mg in 25 mL methanol) was added one shot to $Zn(NO_3)_2$ $6H_2O$ solution (297.5 mg in 25 mL methanol). Being kept still for 5 min, A PVP-Au NRs solution (4 mL) concentrated to 1 mL in methanol by centrifugation (12000 rpm, 5 min) was injected into the above mixed solution. After 24 h, the obtained dark gery precipitate was collected by centrifugation (5000 rpm, 3 min), washed with methanol three times and dried at room temperature for 48 h.

3. Supporting Figures and Tables

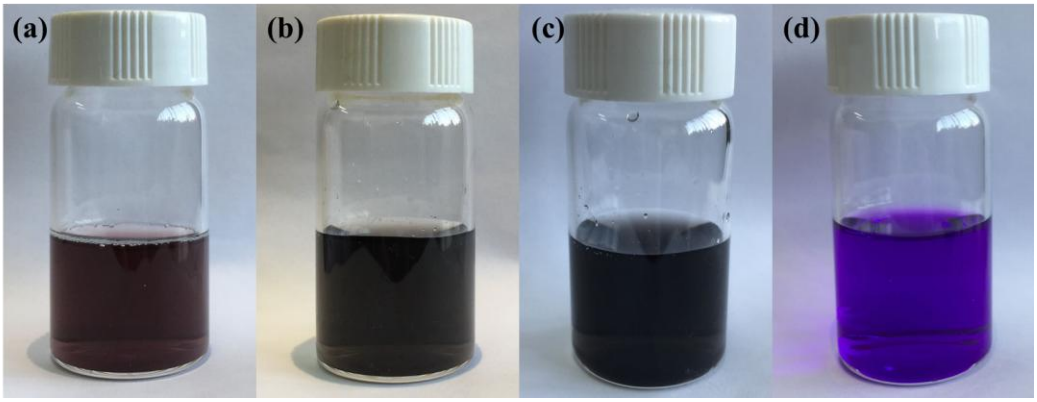

Figure S1. Images of Au NR, Au@Pt NR and Au@Pt NT colloidal solution, related to Figure 2. (a) Au NR colloidal solution, (b) Au@Pt NR colloidal solution, (c) Au@Pt NT colloidal solution, (d) precursor solution of ZIF-67. It is clearly showed that the Pt^{4+} ions are reduced by ascorbic acid for that the color of hydrosol turned form dark red to black.

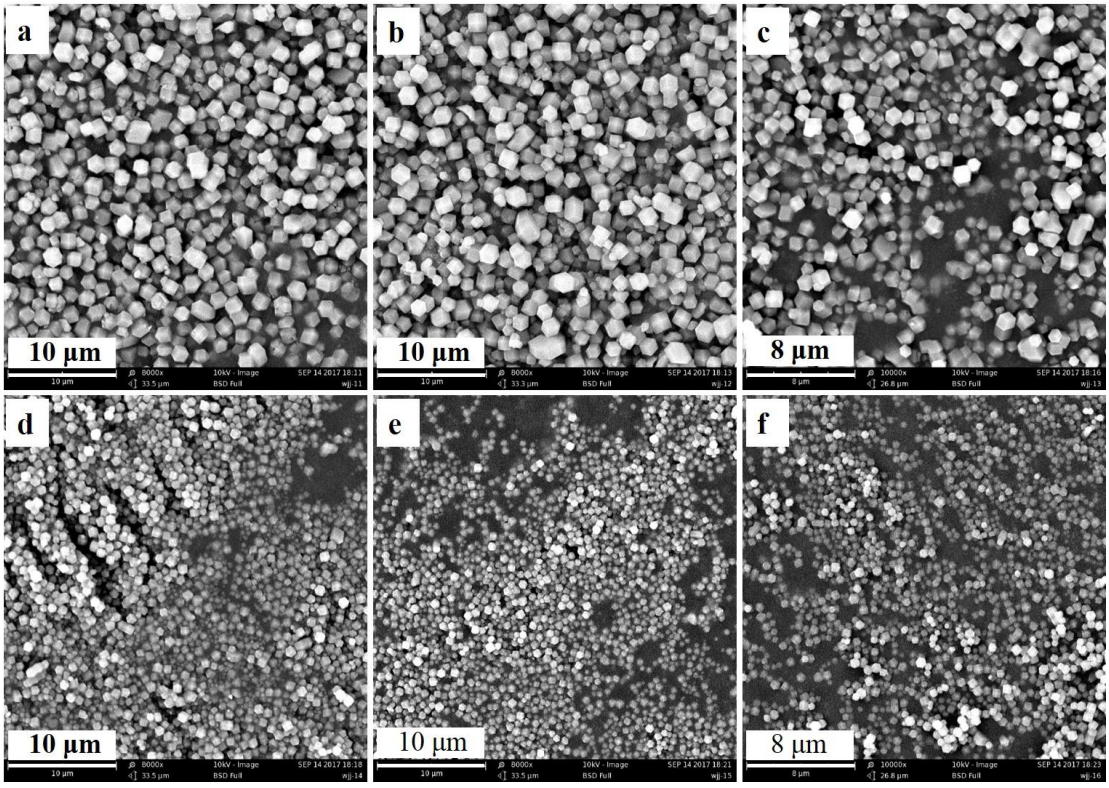

Figure S2. SEM Images of ZIF-67 with different molar ratio of 2-methylimidazole to cobaltous nitrate hexahydrate, related to Figure 2. (a) 3:1, (b) 3.5:1, (c) 4:1, (d) 4.5:1,

(e) 5:1, (f) 5.5:1. Images showed that the size of ZIF-67 particles can be easily modulated by varying the amount of 2-methylimidazole. Considering the both size and crystal yield, the ratio of 4.5 was chosen as the optimal condition, owing to a better homogeneous dodecahedral particle with a size of ~1 μm being obtained.

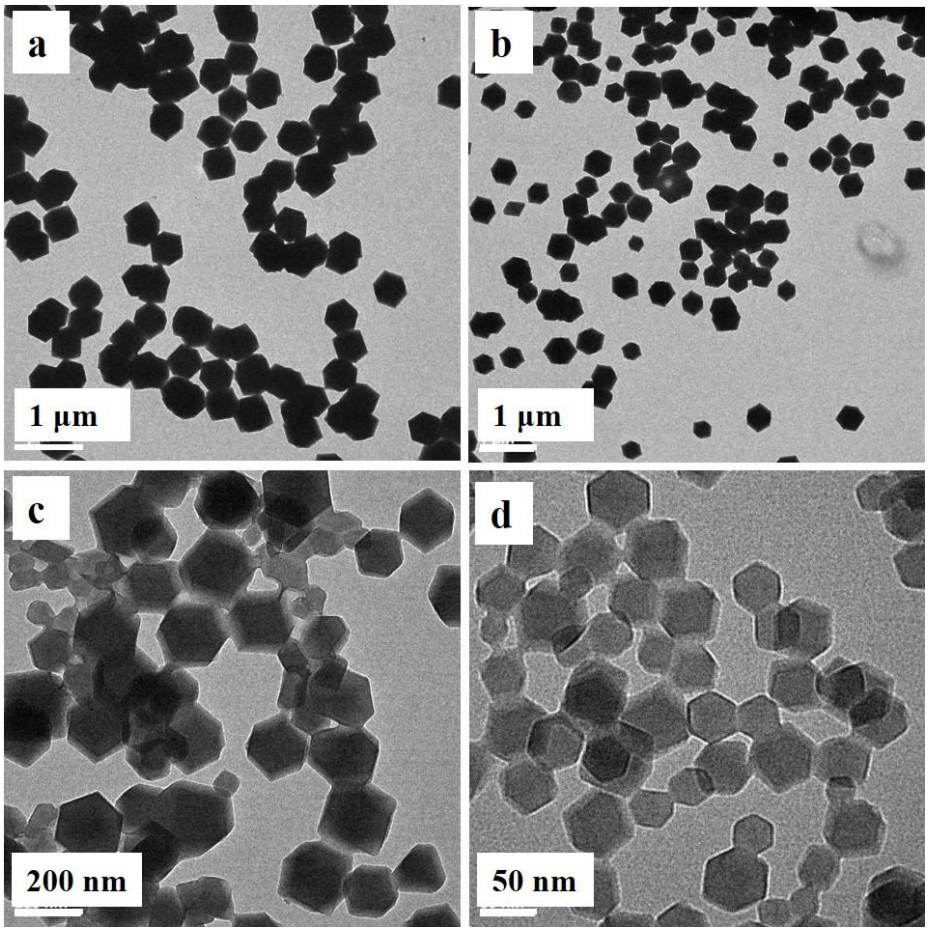

Figure S3. TEM images of ZIF-8 with different molar ratio of 2-methylimidazole to zinc nitrate hexahydrate, related to Figure 2. (a) 1:1; (b) 2:1; (c) 3:1;(d) 4:1. Considering the both size and crystal yield, the ratio of 1 was chosen as the optimal condition, owing to a better homogeneous dodecahedral particle with a size of ~500 nm being obtained.

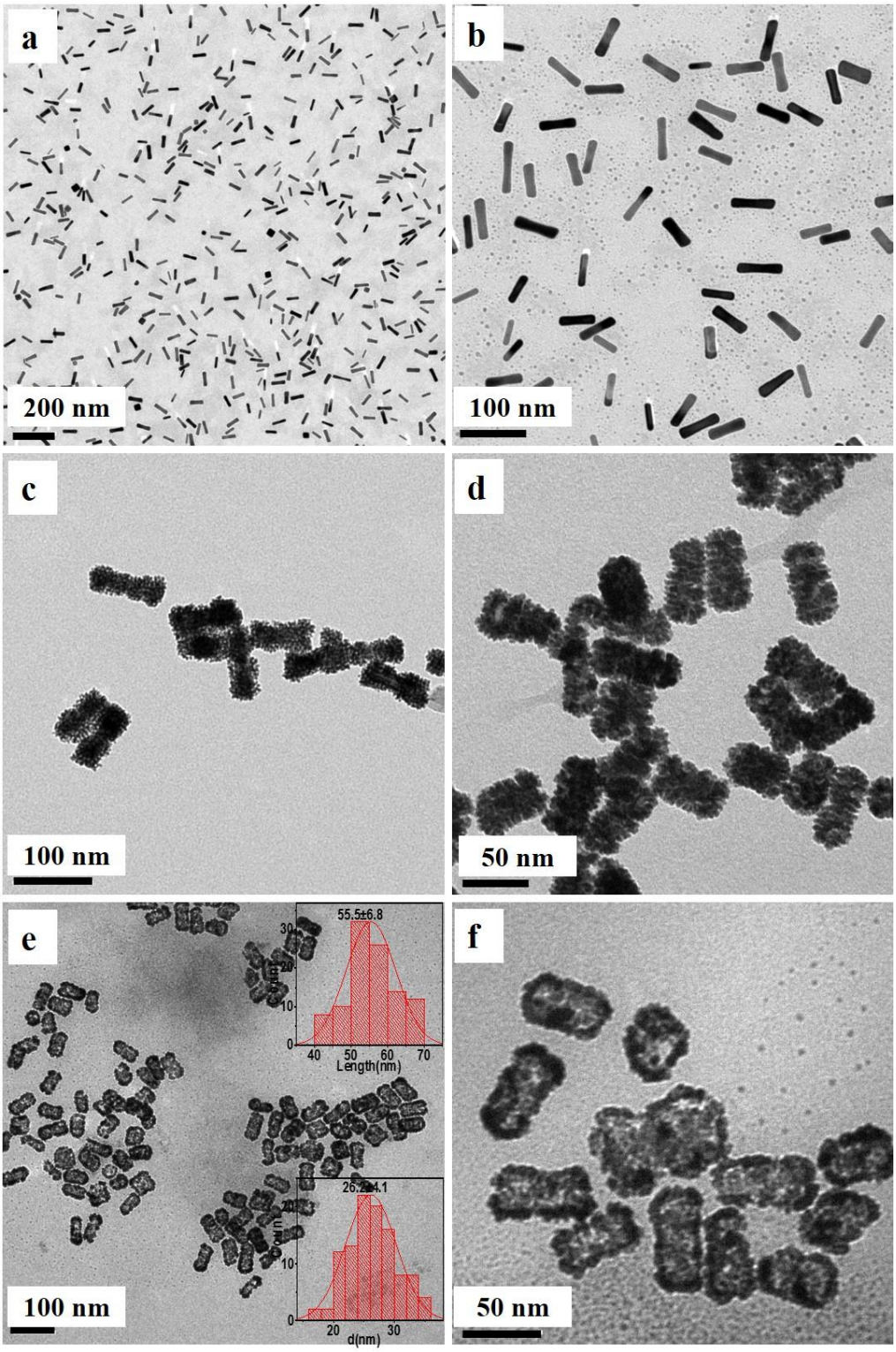

Figure S4. TEM images of Au NRs, Au@Pt NRs and Au@Pt NTs, related to Figure 2. (a, b) Au NRs, (c, d) Au@Pt NRs, (e, f) Au@Pt NTs with an average length of 55.5 nm and an average diameter of 26.2 nm.

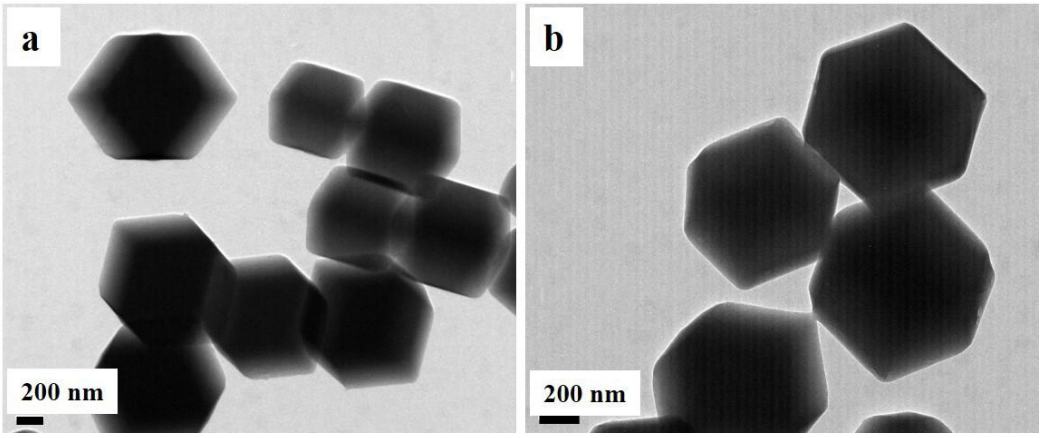

Figure S5. TEM images of ZIF-67, related to Figure 2.

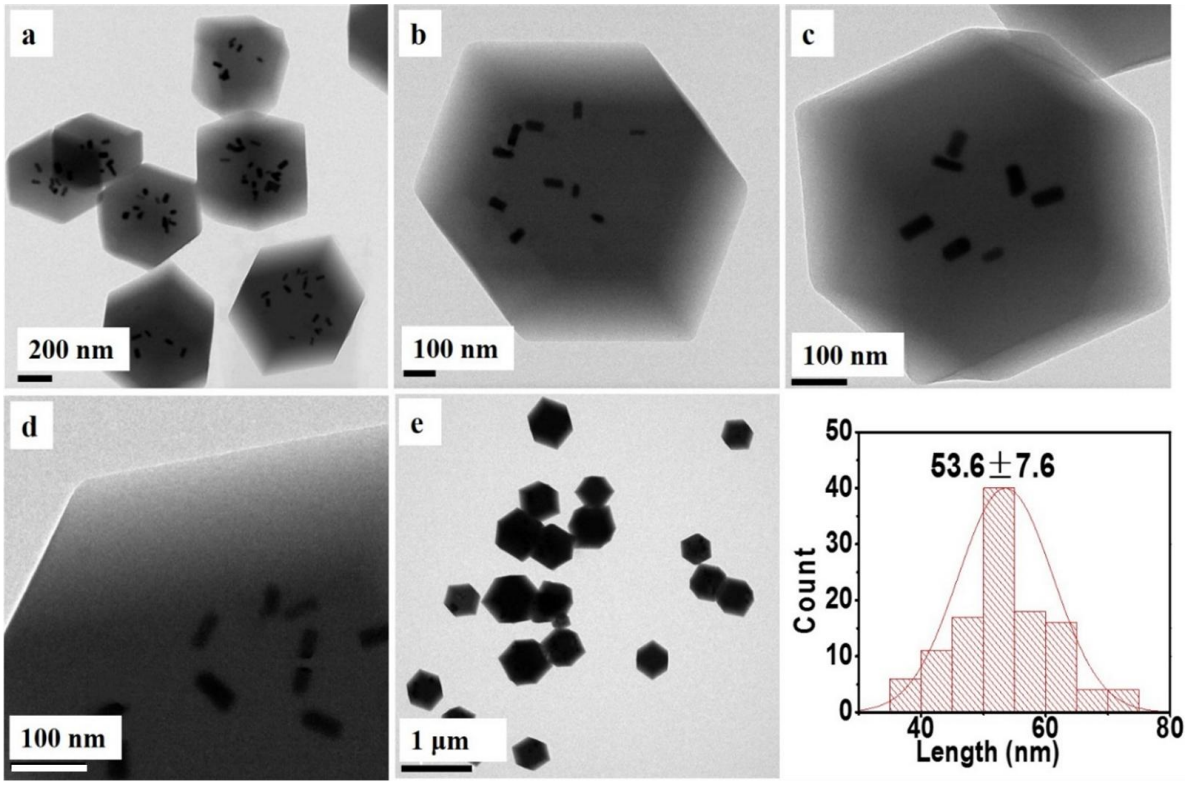

Figure S6. TEM images of Au NRs@ZIF-67 and particle size histogram of Au NRs, related to Figure 2.

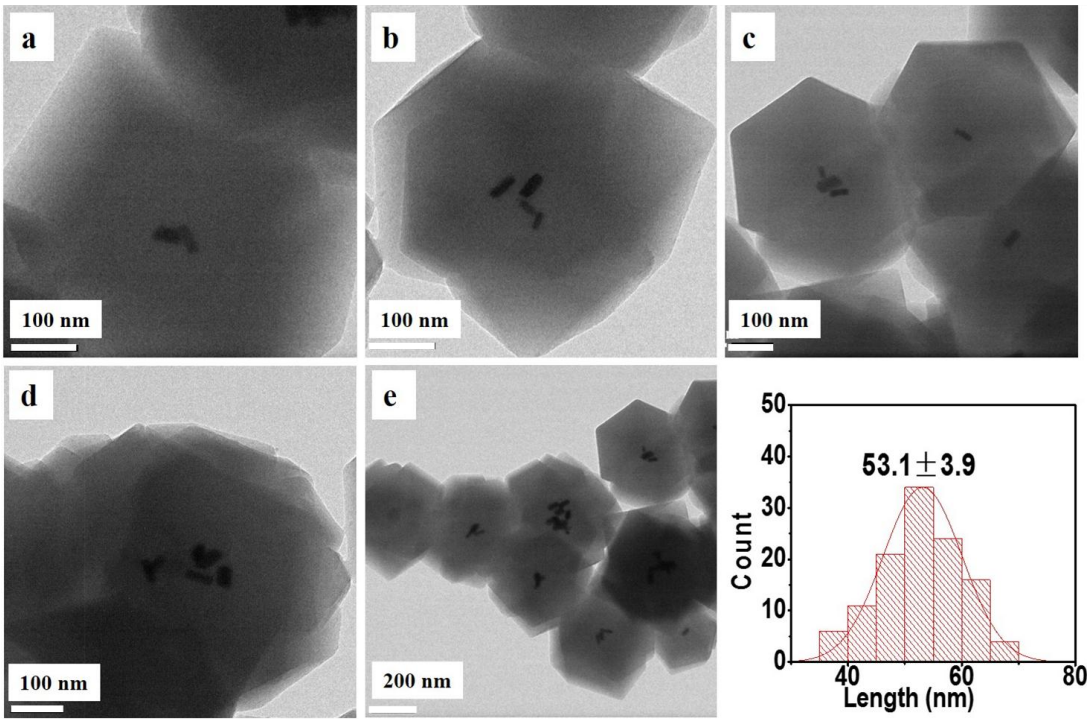

Figure S7. TEM images of Au NRs@ZIF-8 and particle size histogram of Au NRs, related to Figure 2.

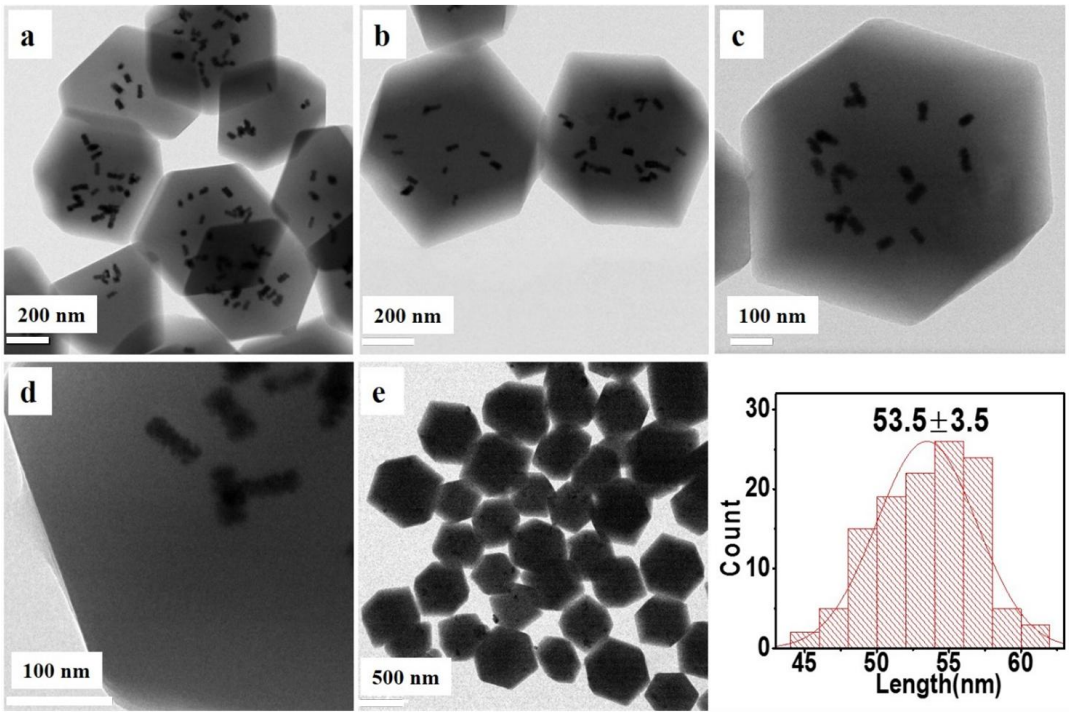

Figure S8. TEM images of Au@Pt NRs@ZIF-67 and particle size histogram of Au@Pt NRs, related to Figure 2.

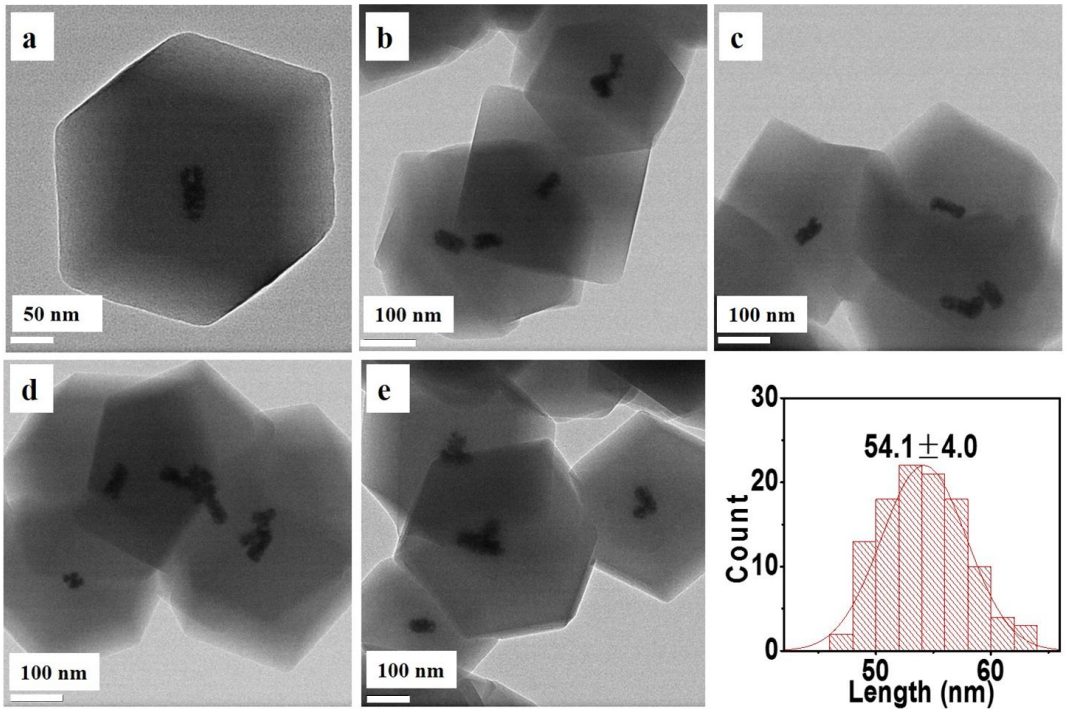

Figure S9. TEM images of Au@Pt NRs@ZIF-8 and particle size histogram of Au@Pt NRs, related to Figure 2.

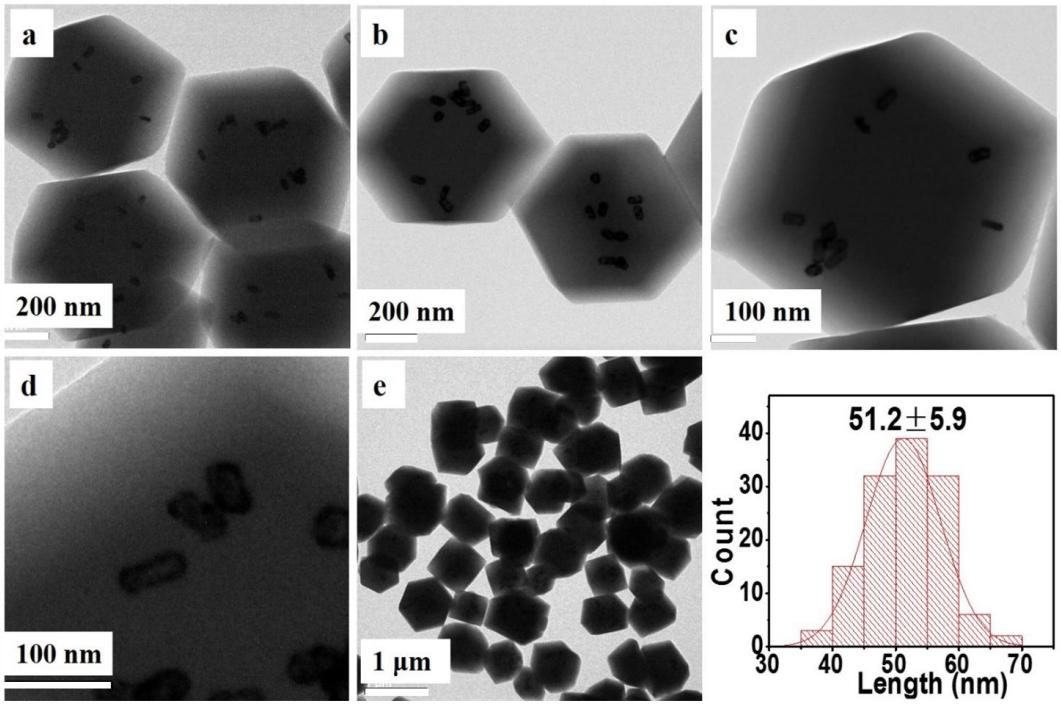

Figure S10. TEM images of Au@Pt NTs@ZIF-67 and particle size histogram of Au@Pt NTs, related to Figure 2.

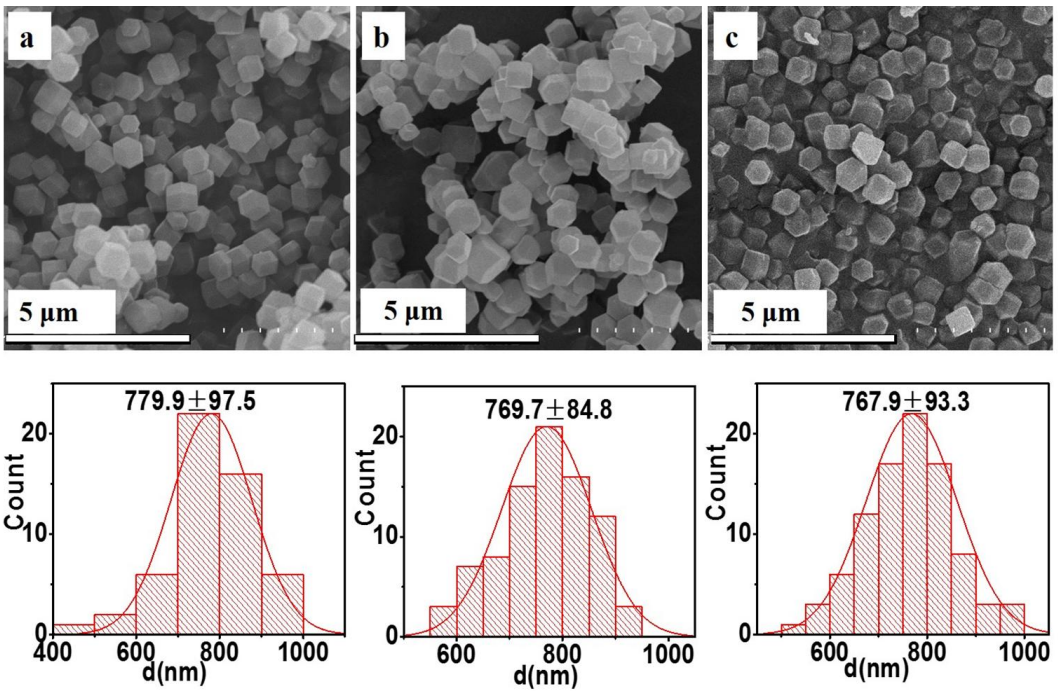

Figure S11. SEM images of composites and corresponding particle size histograms, related to Figure 2. (a) Au NRs@ZIF-67; (b) Au@Pt NRs@ZIF-67; (c) Au@Pt NTs@ZIF-67

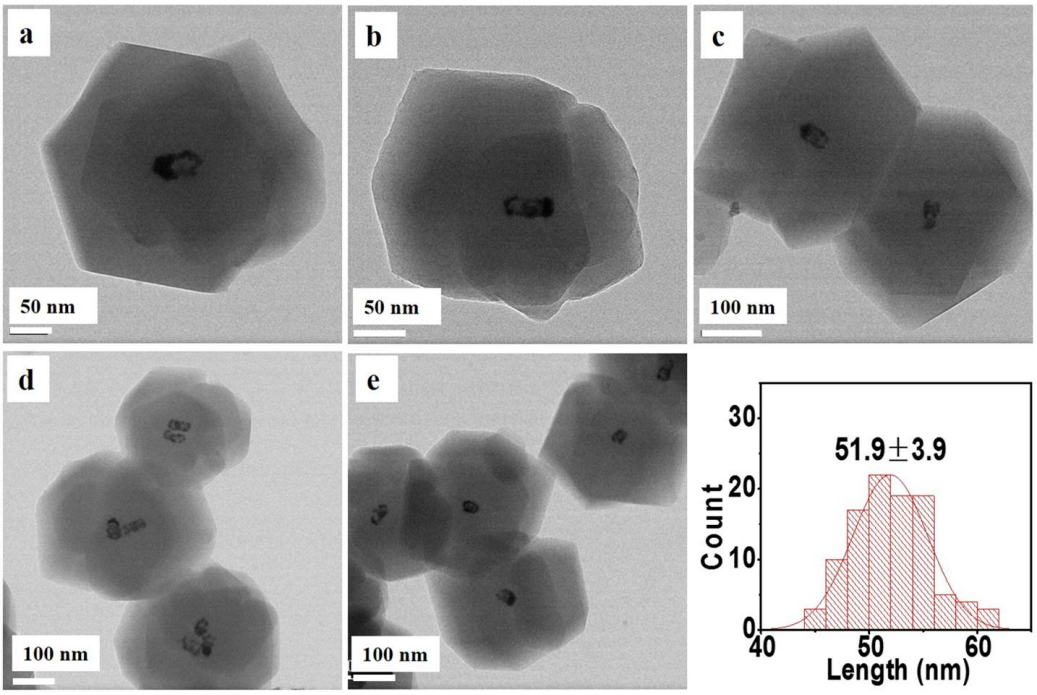

Figure S12. TEM images of Au@Pt NTs@ZIF-8 and particle size histogram of Au@Pt NTs, related to Figure 2.

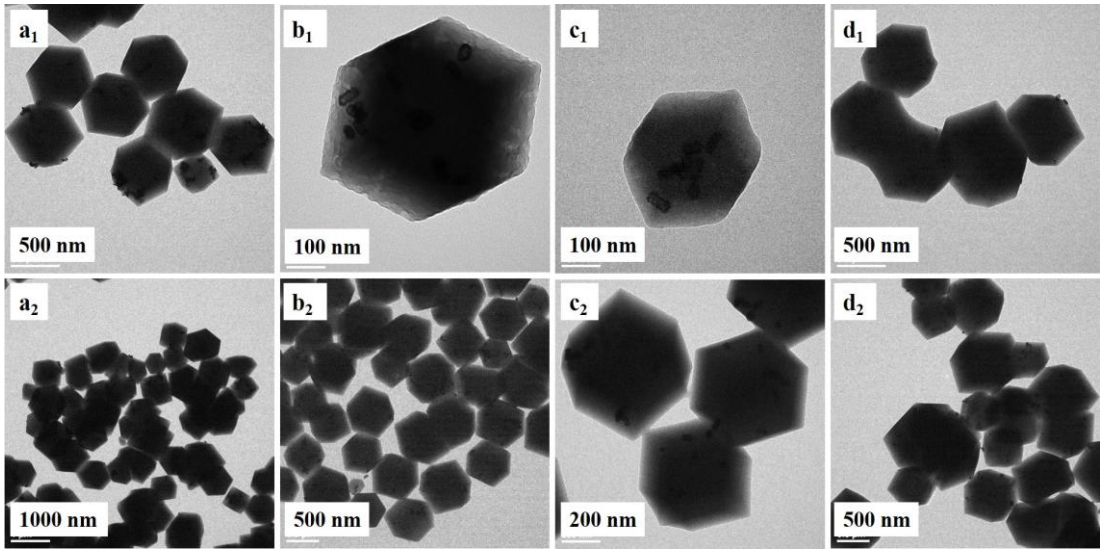

Figure S13. TEM images of Au@Pt NTs@ZIF-67 with different amount of PVP, related to Figure 2. (a) CTAB- Au@Pt NTs, (b) 0 mg, (c) 100 mg, (d) 400 mg. As seen in the images, the encapsulated Au@Pt NTs was increased with the amount of added PVP.

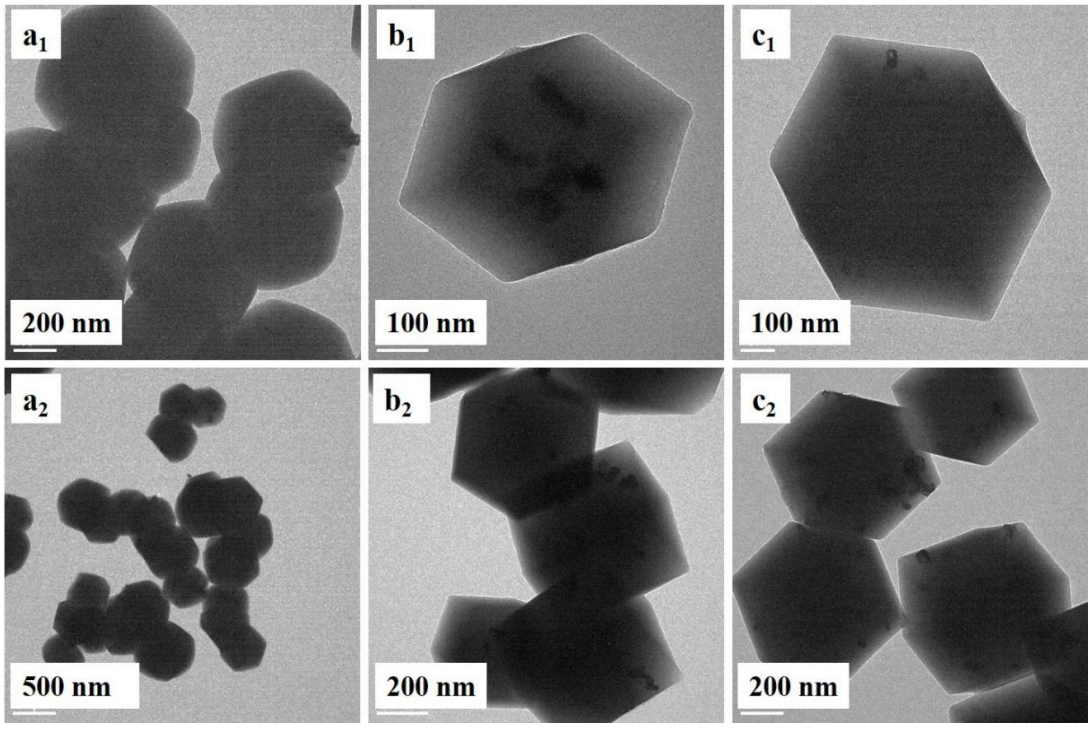

Figure S14. TEM images of Au@Pt NTs@ZIF-67 crystal at different reaction time, related to Figure 2. (a) 30 min, (b) 3h, (c) 8h. When the reaction is 3 h, the structure of product was nearly as same as the product of 24 h, the reaction is completed.

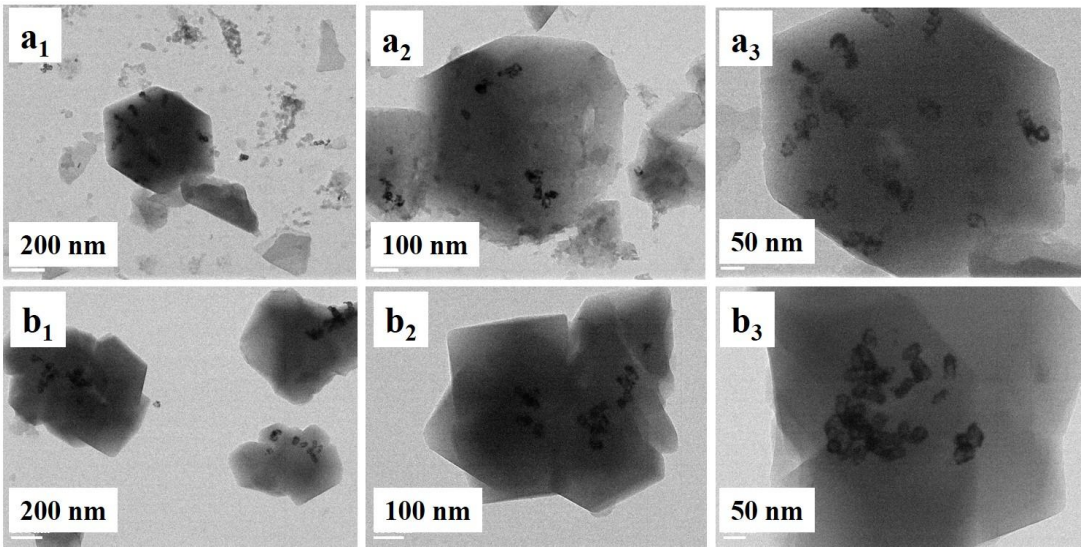

Figure S15. TEM images after catalysis: (a) Au@Pt NTs@ZIF-67; (b) Au@Pt NTs@ZIF-8, related to Figure 4.

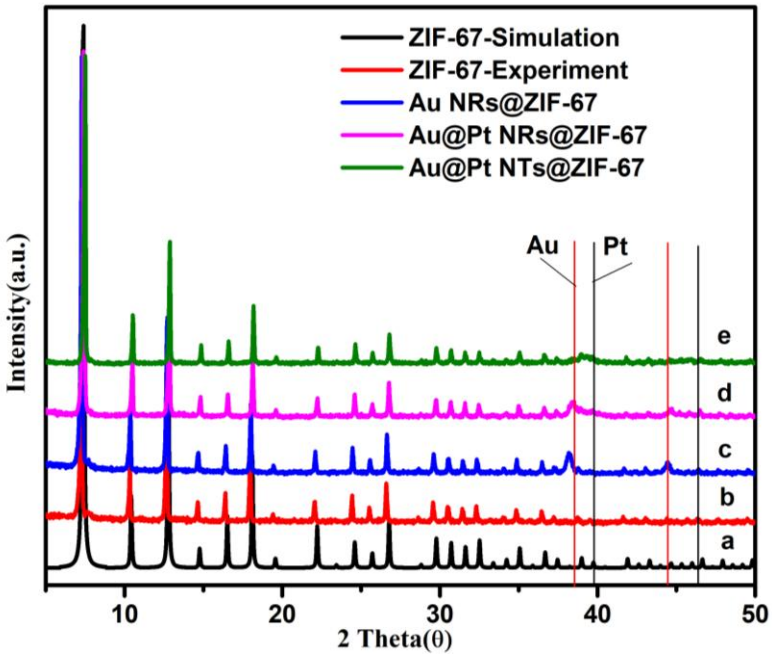

Figure S16. Powder XRD patterns of different products, related to Figure 2. (a) simulated ZIF-67, (b) ZIF-67, (c) Au NRs@ZIF-67, (d) Au@Pt NRs@ZIF-67, (e)Au@Pt NTs@ZIF-67.

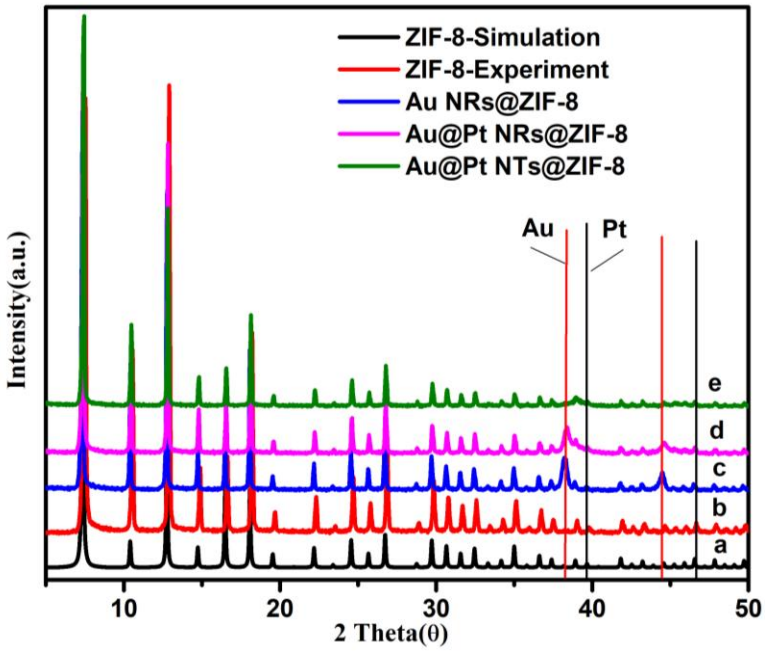

Figure S17. Powder XRD patterns of different products, related to Figure 2. (a) simulated ZIF-8, (b) ZIF-8, (c) Au NRs@ZIF-8, (d) Au@Pt NRs@ZIF-8, (e)Au@Pt NTs@ZIF-8.

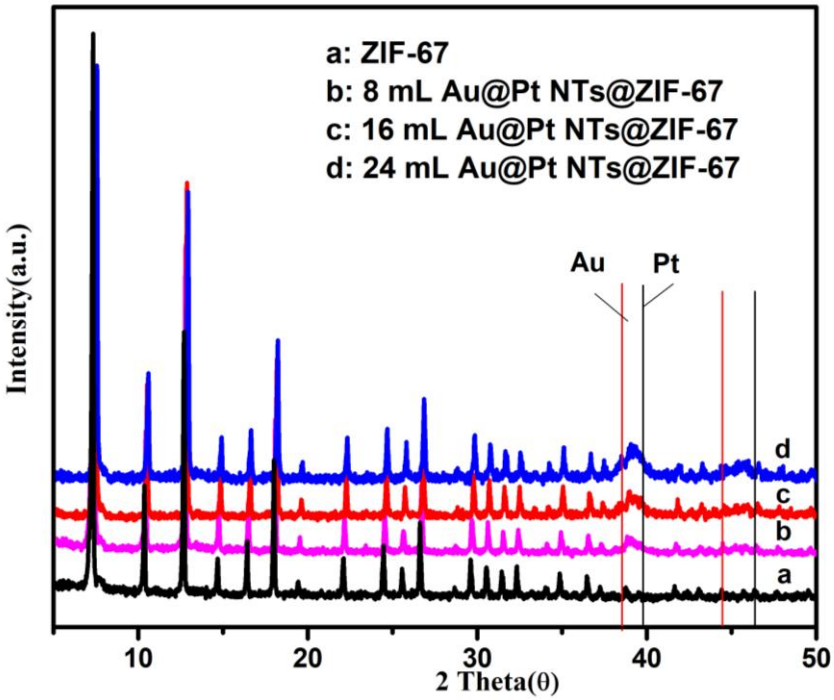

Figure S18. Powder XRD patterns of Au@Pt NTs@ZIF-67 with different amount of Au@Pt NTs, related to Figure 2. (a) ZIF-67, (b) 8 mL, (c) 16 mL, (d) 24 mL.

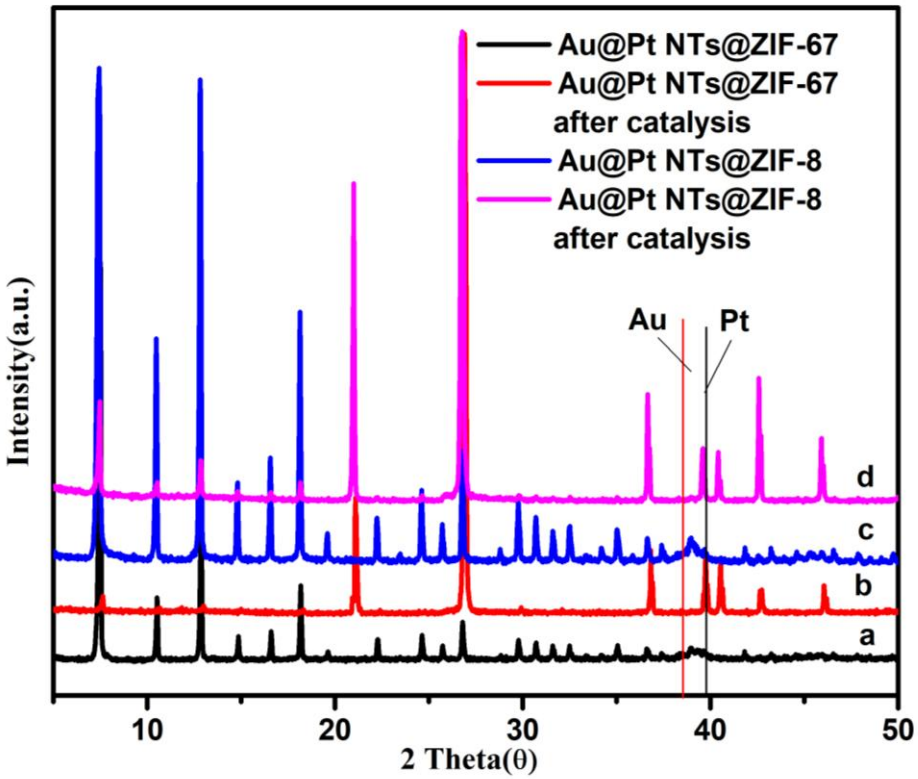

Figure S19. Powder XRD patterns of catalysts, related to Figure 4. (a) Au@Pt NTs @ZIF-67, (b) Au@Pt NTs@ZIF-67 after catalysis, (c) Au@Pt NTs@ZIF-8, (d) Au@Pt NTs@ZIF-8 after catalysis. As shown in Figure, PXRD pattern peaks at 2theta=20.859, 26.639, 36.534, 39.464, 40.299, 42.449, 45.792 owing to SiO_2 (quartz sand), which is so strong that the MOF peak appears weak.

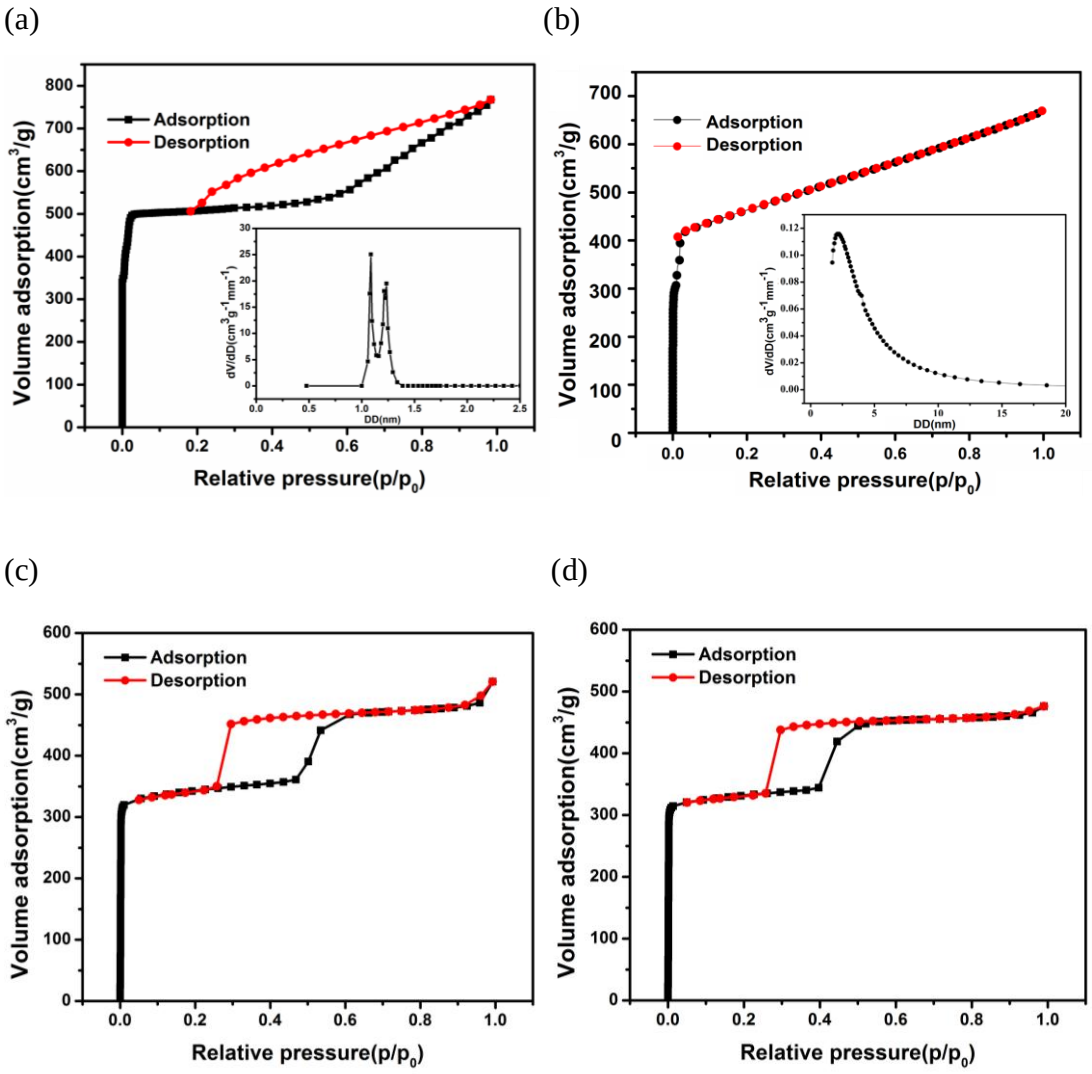

Figure S20. N_2 adsorption–desorption isotherms of the different nanocomposites, related to Figure 2. (a) ZIF-67, (b) Au@Pt NTs@ZIF-67, (c) ZIF -8, (d) Au@Pt NTs@ZIF-8. BET Surface Areas were 1547.5, 1543.6, 918.5 and 888.5 m^2g^{-1}, respectively.

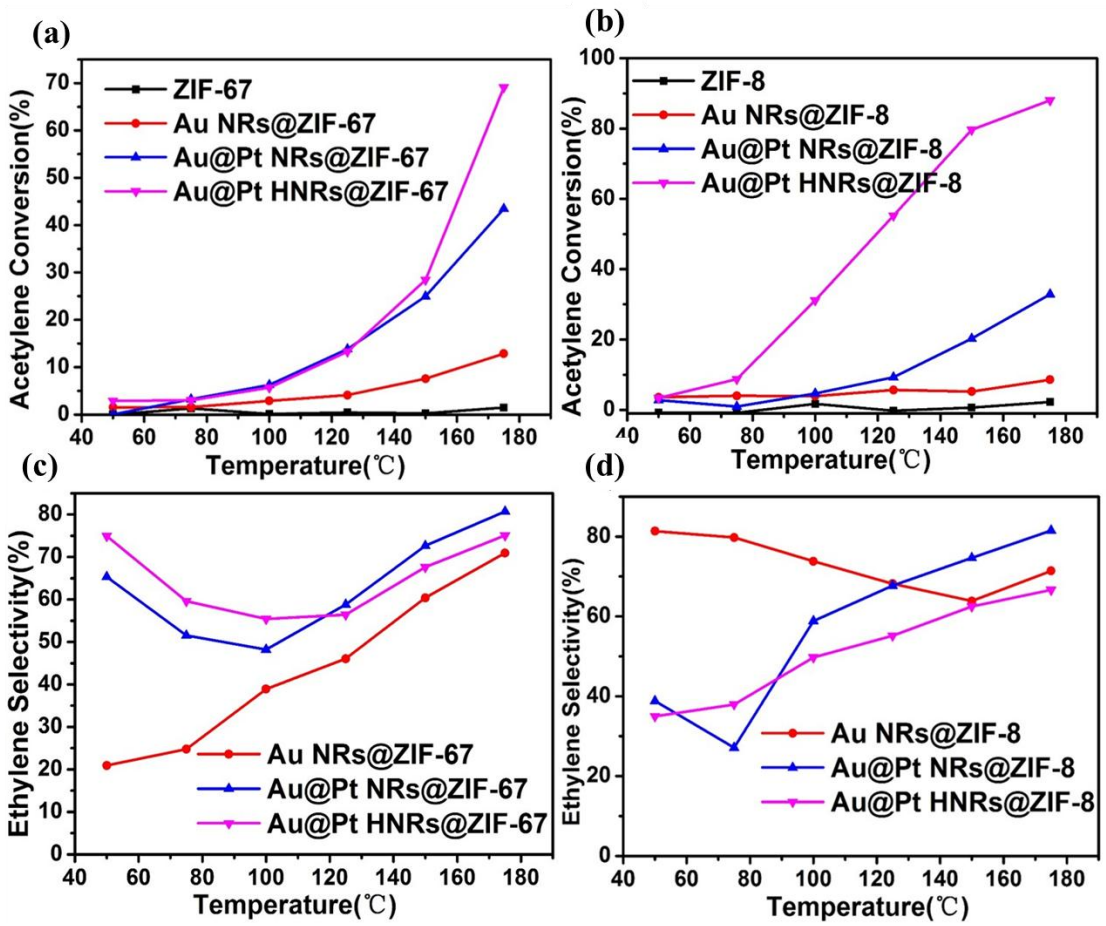

Figure S21. Acetylene conversion and ethylene selectivity, related to Figure 4. Acetylene conversion by (a) NPs@ZIF-67 and (b) NPs@ZIF-8. Ethylene selectivity by (c) NPs@ZIF-67 and (d) NPs@ZIF-8.

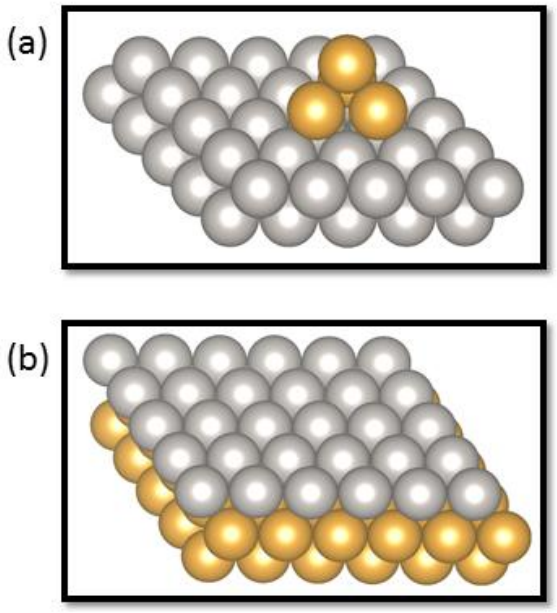

Figure S22. Constructed model, related to Figure 5. (a)Au@Pt NTs and (b)Au@Pt NRs. Orange is gold atom and grey is platinum.

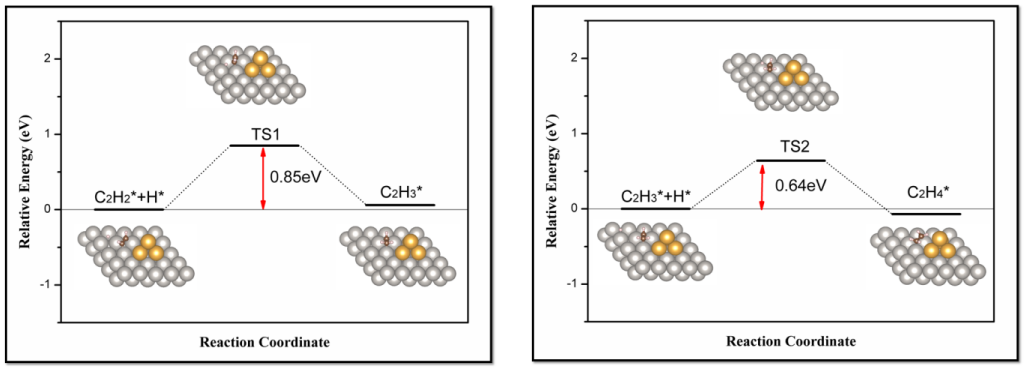

Figure S23. Energetics diagram of C_2H_2 hydrogenation to C_2H_4 on Au@Pt NTs, related to Figure 5. Brown is carbon atom, white is hydrogen, orange is gold and grey is platinum.

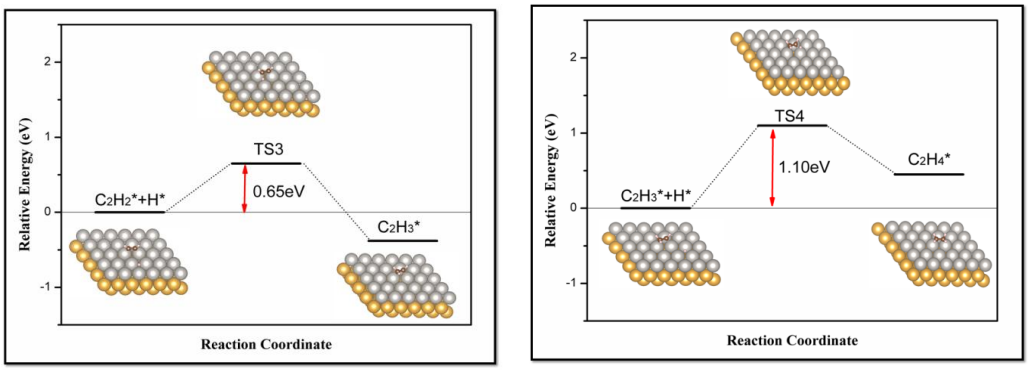

Figure S24. Energetics diagram of C_2H_2 hydrogenation to C_2H_4 on Au@Pt NRs, related to Figure 5. Brown is carbon atom, white is hydrogen, orange is gold and grey is platinum.

Table S1. Deposition efficiency of Au@Pt NTs content supported within ZIF-67 and ZIF-8, related to Figure 2 and 4.

Catalysis	Nominal loading (wt %)a		Actual loading (wt%)b	
	Pt	Au	Pt	Au
Au@Pt HNTs@ZIF-67	2.2%	-	0.90%	0.84%
Au@Pt HNTs@ZIF-8	3.75%	-	2.5%	2.1%
Au@Pt NRs@ZIF-67	2.2%	3.2%	1.3%	2.6%
Au@Pt NRs@ZIF-8	3.75%	4.75%	2.9%	4.5%
AuNRs@ZIF-67	-	3.2%	-	3.0%
AuNRs@ZIF-8	-	4.75%	-	4.4%

[a] Determined by loading amount of metal precursors.

[b] Determined by inductively coupled plasma atomic emission spectroscopy (ICP-AES) analysis.

Table S2. The performance of various MOFs for semi-hydrogenation of acetylene, related to Figure 4.

Catalyst	dosage	Temperature/ ^{o}C	Conversion	Selectivity	Yield	Ref.
Au-250	33 mg	250	< 10%	99%	< 10%	Shun et al., 2015
Pd-250	33 mg	175	~ 100%	~10%	10%	Shun et al., 2015
Pd-250	33 mg	200	~100%	~30%	30%	Shun et al., 2015
AuPd-250	33 mg	175	~35%	~90%	31.5%	Shun et al., 2015
AuPd-250	33 mg	200	~40%	~90%	36.0%	Shun et al., 2015
AuPd-250	33 mg	250	~50%	~90%	45.0%	Shun et al., 2015
Pd/Al_2O_3	1 mg	52	12%	42%	5.04%	Gonçalves et al., 2020
$Pd_{20}Ag_{80}$	50 mg	200	83%	49%	40.67%	Osswald et al., 2008
Pd/Al_2O_3	50 mg	200	17%	43%	7.3%	Osswald et al., 2008
Pd NPs/C	50 mg	130	~95%	~15%	14.25%	Yang et al., 2015
Pd@H-Zn/Co-ZIF	50 mg	130	~100%	~17%	17.0%	Yang et al., 2015
CuNPs@NU-1000	10 mg	200	20%	97%	19.4%	Redfern et al., 2018
Au@Pt NTs@ZIF-67	50 mg	175	69.1%	71.39%	49.3%	This work
Au@Pt NTs@ZIF-8	50 mg	175	88%	66.63%	58.6%	This work

REFERENCES

Gonçalves, L. P. L.; Wang, J.; Vinati, S.; Barborini, E.; Wei, X.-K.; Heggen, M.; Franco, M.; Sousa, J. P. S.; Petrovykh, D. Y.; Soares, O. S. G. P.; Kovnir, K.; Akola, J.; Kolen'ko, Y. V. (2020). Combined experimental and theoretical study of acetylene semi-hydrogenation over Pd/Al_2O_3. Int. J. Hydrogen Energ. 45 (2), 1283-1296.

Osswald, J.; Kovnir, K.; Armbruster, M.; Giedigkeit, R.; Jentoft, R. E.; Wild, U.; Grin, Y.; Schlogl, R. (2008). Palladium – gallium intermetallic compounds for the selective hydrogenation of acetylene Part II: Surface characterization and catalytic performance. J. Catal. 258 (1), 219-227.

Redfern, L. R., Zhanyong, L., Xuan, Z., & Farha, O. K. (2018). Highly Selective Acetylene Semihydrogenation Catalyzed by Cu Nanoparticles Supported in a Metal–Organic Framework. ACS Appl. Nano Mater. 1, 4413-4417.

Shun, Z., Chen, C., Jang, B. W.-L., Zhu, A. (2015). Radio-frequency H_2 plasma treatment of $AuPd/TiO_2$ catalyst for selective hydrogenation of acetylene in excess ethylene. Catalysis Today 256, 161-169.

Yang, J., Zhang, F., Lu, H., Hong, X., Jiang, H., Wu, Y. and Li, Y. (2015). Hollow Zn/Co ZIF Particles Derived from Core–Shell ZIF-67@ZIF-8 as Selective Catalyst for the Semi-Hydrogenation of Acetylene. Angew. Chem. Int. Ed. 54, 10889-10893.